AN EXPERIMENTAL AND NUMERICAL INVESTIGATION OF BIMODAL PARTICLE DISTRIBUTIONS FOR ENHANCED THERMAL CONDUCTIVITY IN CONCENTRATING SOLAR POWER APPLICATIONS

by

Dallin Daniel Stout

A thesis

submitted in partial fulfillment

of the requirements for the degree of

Master of Science in Mechanical Engineering

Boise State University

August 2023

BOISE STATE UNIVERSITY GRADUATE COLLEGE

DEFENSE COMMITTEE AND FINAL READING APPROVALS

of the thesis submitted by

Dallin Daniel Stout

Thesis Title:	An Experimental and Numerical Investigation of Bimodal Particle Distributions for Enhanced Thermal Conductivity in Concentrating Solar Power Applications
Date of Final Oral Examination:	21 April 2023

The following individuals read and discussed the thesis submitted by Dallin Daniel Stout, and they evaluated the student's presentation and response to questions during the final oral examination. They found that the student passed the final oral examination.

Todd Otanicar, Ph.D.	Chair, Supervisory Committee
Krishna Pakala, Ph.D.	Member, Supervisory Committee
Nirmala Kandadai, Ph.D.	Member, Supervisory Committee

The final reading approval of the thesis was granted by Todd Otanicar, Ph.D., Chair of the Supervisory Committee. The thesis was approved by the Graduate College.

ACKNOWLEDGMENTS

I would like to acknowledge Dr. Todd Otanicar, my advisor, for his guidance these last two years. I would like to acknowledge Dr. Krishna Pakala, my Advanced Fluid Mechanics teacher, for his excellent teaching ability that allowed me to understand complex fluids concepts. I would also like to acknowledge Dr. Nirmala Kandadai for her monthly advisement and input concerning my research into particle thermal conductivity enhancement.

ABSTRACT

Solid particles have recently attracted substantial interest as a thermal transport medium in high-temperature energy storage and thermal energy conversion systems due to their ability to operate at high temperatures (up to 1000 °C). This is especially useful in the concentrating solar power (CSP) industry where solid particles are utilized as heat transfer media. Thermal conductivity of particles in CSP is critically important to the overall heat transfer that occurs within a heat exchanger. A cheap and effective avenue to increase the thermal conductivity of a particle distribution is by reducing its porosity by employing 2 differently sized particles. The thermal conductivity can be increased further by applying a load to the particles. At lower temperatures (20-300 °C), previous work has demonstrated a binary particle distribution has superior thermal conductivity. In this work, the thermal conductivities of HSP binary particle distributions under load are explored at ambient temperatures revealing enhanced thermal conductivity. Furthermore, high temperature (from 300-700 °C) analysis of HSP binary particle distributions are also explored with results being that monodispersed distributions yield higher thermal conductivities due to enhanced surface radiation in larger particles. A bimodal distribution increases packed-bed thermal conductivity only up to around ~400 °C at which monodisperse distributions with larger particles then yield higher thermal conductivities. HSP binary particle thermal conductivity results are compared to current models demonstrating inadequate characterization at high temperatures (>400 °C) due to the dominant heat transfer mechanism of radiation in larger particles at high temperature.

These models are implemented in a numerical model of the Gen3 Particle Pilot Plant (G3P3) 20 kW_t prototype heat exchanger constructed by Sandia National Laboratory (SNL) where they can then be validated using SNL's experimental data from the prototype. From SNL's experimental data, the ZBS thermal conductivity method is confirmed to be accurate at working G3P3 20 kW_t prototype heat exchanger temperatures (290-500 °C) at particle and sCO_2 mass flow rates of 100 g/s while the Yagi and Kunii thermal conductivity method is not. Utilizing the validated numerical model and ZBS thermal conductivity method, various binary particle mixtures are simulated at working G3P3 20 kW_t prototype heat exchanger temperatures revealing increases in the overall heat transfer coefficient of up to 25% in HSP 16/30-40/70 mixtures as well as increases as high as 40% in CP 20/40-70/140 mixtures when compared to monodispersed particle distributions of the respective mixtures' large particles. Solid particle thermal conductivity enhancement with binary particle distributions in this way has the potential to be a significant step forward towards the CSP industry's goal of developing the world's first 1 MW_t heat exchanger through the G3P3 program.

TABLE OF CONTENTS

LIST OF TABLES

LIST OF FIGURES

LIST OF ABBREVIATIONS

BSU	Boise State University
CP	Ceramic Proppant
CSP	Concentrating Solar Power
FPR	Falling Particle Receiver
G3P3	Gen 3 Particle Pilot Plant
HSP	High-Strength Proppant
MAC	Measurement Acceptability Criteria
MS	Molten Salt
SNL	Sandia National Laboratory
sCO_2	Supercritical Carbon Dioxide
TES	Thermal Energy Storage
TPS	Transient Plane Source

CHAPTER ONE: INTRODUCTION

1.1 Concentrating Solar Power: A History and Introduction

Concentrating solar power (CSP) was not always utilized as a clean, renewable energy source. Long ago, in one of the first recorded CSP events in history, it was used in the defense of one's country.

1.1.1 CSP in History

In 212 B.C., Marcellus of Rome laid siege to the great philosopher Archimedes' city of Syracuse with his command of an entire fleet of ships during the Second Punic War [1]. Archimedes, primarily heralded for his works in physics and mathematics, invented many devastating mechanical weapons that could be utilized in the defense of Syracuse. One of these, was the use of 'burning mirrors' or reflective parabolic plates forged from flat metal [2]. When the parabolic mirrors were focused on the attacking ships, the concentrated sunlight increased the surface temperature of the attacking vessels to the point of combustion as can be seen by a wall painting completed in 1600 by Stanzino delle Matematiche in Figure 1.1. While controversial in validity, this historical event was one of the first regarding concentrating solar power.

Figure 1.1 Wall painting from the Uffizi Gallery, Stanzino delle Matematiche, in Florence, Italy, showing the Greek mathematician Archimedes' mirror being used to burn Roman military ships in the Battle of Syracuse.

1.1.2 CSP and Molten-Salt Heat Transfer Media

Archimedes' use of CSP for defense tactics is a historically isolated event. Since the Battle of Syracuse, CSP has transitioned from a defense tactic into a sophisticated method to extract clean, limitless energy. In 1866, Auguste Mouchout developed parabolic troughs to heat water and then produce steam that was used in the first solar-steam engine [3]. Mouchout's work was then foundational in the establishment of an Egyptian farming community by Frank Schuman who used the troughs to produce steam that drove water pumps through the harsh desert climate [4]. The 1950s saw the development of molten salts (MS) for use as heat transfer fluid by Oak Ridge National Laboratory in nuclear powered aircraft and eventually nuclear reactors [5]. Then, in 1968, Professor Giovanni Francia produced the first operational CSP plant in Sant'llario Italy that is similar to CSP plants today in that a singular, central receiver is surrounded by a field of solar collectors [6]. In

1993, the first CSP plant to use MS for energy storage was Solar Two, located in the Mojave Deseret of California [5].

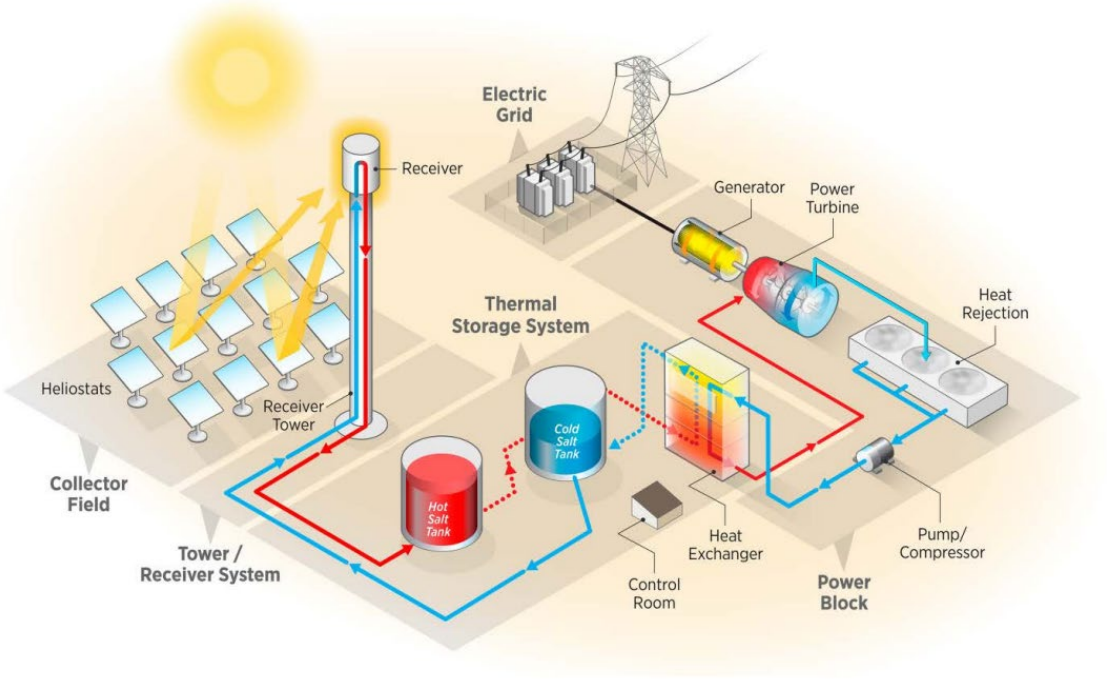

Figure 1.2 Molten-salt power tower with direct storage of salt. Adopted from [7]**.**

Figure 1.2 displays an MS power tower based on the design of Solar Two. These power towers operate by heating MS by reflecting and concentrating sunlight onto a receiver. The heated MS is then stored in a Hot Salt Tank until it is driven through a heat exchanger. The heat from the MS is transferred into a working fluid which then will aid in the generation of steam for use in a Power Turbine. The Power Turbine then generates electricity for a power grid [7]. The 1990's saw frequent use of MSs as heat transfer media in CSP applications but solid particles have recently attracted significant attention as an efficient alternative [8]. CSP facilities are currently exploring MS additives to improve working

temperatures and overall thermal energy storage (TES) performance; however, these additives are not cost effective [9].

1.2 Solid Particles as Heat Transfer Media in CSP

Traditional MS-based media is limited to temperatures of ~600 °C [8]. Solar thermal facilities such as that of the falling particle receiver (FPR) concentrate sunlight from a large number of heliostats and can irradiate media well beyond the 600 °C threshold [8].

1.2.1 CSP and Solid Particle Heat Transfer Media

An FPR receiver can be seen in Figure 1.3. This solar thermal facility uses conveyer-like operations to drop solid particles through an open aperture where they are quickly and effectively irradiated. These heated particles are stored in a Hot Silo until they are funneled through a Particle Heat Exchanger to transfer their thermal energy into a working fluid. They are then dropped into a Cold Silo and await conveyance to again be irradiated and heated [7]. In these systems, solid particles have the benefit of being able to be heated to temperatures upwards of 1000 °C [10], well beyond the temperature limitations of conventional MS systems. Sand and proppants, commonly employed in the oil and gas industry in fracking operations and as casting media in foundry applications, have been identified as alternative heat transfer media candidates in solar thermal facilities due to their low cost, high durability, and capacity to withstand temperatures superseding 1000 °C [8].

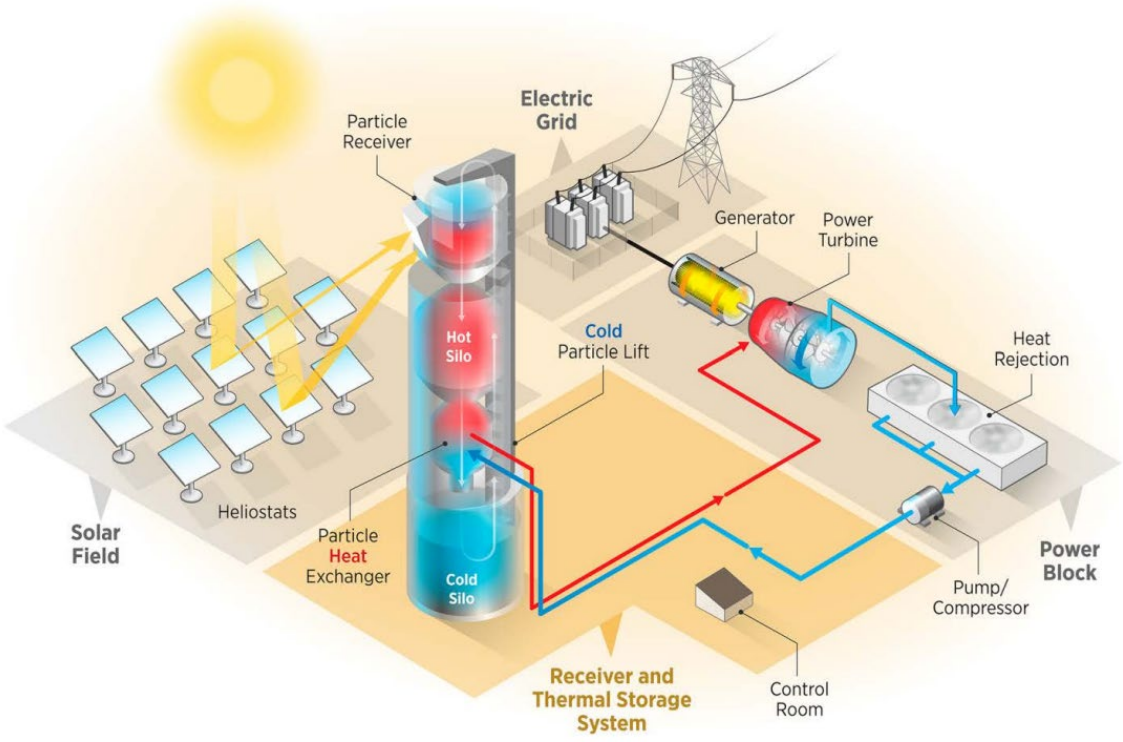

Figure 1.3 Falling-particle receiver system with integrated storage and heat exchange for a power cycle. Adopted from [7]**.**

A driving factor in the effectiveness of a solar thermal facility is the thermal conductivity of the heat transfer media implemented [11]. The thermal conductivity of the heat transfer media should be optimized for maximum overall efficiency and minimal cost. The importance of thermal conductivity in a solar thermal facility is illustrated by the work of Albrecht and Ho [12] in their analysis of moving packed-bed shell-and-plate particle-to-sCO_2 heat exchangers [12]. Through a dense, granular flow of particles, the thermal conductivity of a particle distribution can be transferred into a working fluid, such as sCO_2, which ultimately drives advanced power cycles.

1.2.2 Optimizing Solid Particle Heat Transfer Media

The performance of solid particles are still being researched and investigated for their ability to provide cheap, effective thermal transport in solar thermal facilities [13]. Natural

granular and ceramic materials have been experimentally characterized with the intention of being used as heat transfer media [8]. Quartz sand is an economically viable option but possesses poorer thermophysical and thermomechanical characteristics than ceramic particles which are able to entirely withstand the rigors of thermal cycling [14]. The thermal conductivity of ceramic particles has been examined with many different measurement techniques, one being the transient hot-wire (THW) method [15]. This method was implemented on ceramic particles from room temperature up to 700 °C in both air and N_2 gases revealing that gas conduction is a significant heat transfer contributor at higher temperatures [15].

Theoretically, thermal conductivity can be optimized by material selection [16], high-emissivity coatings [17], larger particle diameters [18] or applied force [19]. While particles composed of sand or ceramic-like materials have significantly lower thermal conductivities when compared to other TES materials like aluminum [20], they are often utilized because they are considerably cheaper. Researchers have studied coating particles in high-emissivity substances [21], however, the effects of abrasion and particle wear indicate that it could limit particle-use longevity [22]. Larger particle diameters have superior thermal conductivity values when compared to smaller diameters [18], however, they are not always ideal as some design and operating considerations for the particle-to-sCO_2 shell-and-plate heat exchangers suggest that optimal heat transfer occurs with particle channel widths of 4 mm and limited particle sizes of 200 μm [11]. Furthermore, larger particle diameters greater than 700 μm have the potential to cause unstable particle flows resulting in inefficient solar radiation heat transfer in certain heat exchanger configurations [7]. Applied force is a relatively new tactic that has only been briefly examined with powders [19]. One study found

that applied force increases asymptotically with the thermal conductivity of a powder. Theoretically, the same phenomena would occur when applied to particles, however, this has not yet been tested.

A new and innovative approach to improving the thermal conductivity of a particle distribution is by adding another particle size and thus creating a binary particle mixture [23]. This effectively reduces the porosity of the particle mixture and improves its thermal conductivity. Christen et al. [23] demonstrated that for a variety of ceramic particle distributions composed of particles manufactured by CARBOBEAD, binary particle distributions yield superior thermal conductivities up to 300 °C.

Christen et al. [23] also compared their experimental data with two different porosity models: Standish and Yu [24] and Chang and Deng [25] with the latter being determined as more accurate. Furthermore, these researchers then utilized the two porosity models as inputs for two thermal conductivity models: Zehner, Bauer and Schlunder (ZBS) [26], and Yagi and Kunii [27]. Both models roughly predicted the thermal conductivity behaviors of the evaluated particle distributions with either porosity model [23].

1.3 Research Scope and Objective

The objective of this work to is determine the heat transfer effectiveness of binary particle distributions at high temperature. This work is the first to examine the thermal conductivity of binary particle distributions at temperatures up to 700 °C and also the first to examine the relationship between applied force and thermal conductivity of binary particle distributions which could positively impact particle TES systems utilized in CSP applications. The experimental data will be compared with the ZBS and Yagi and Kunii thermal conductivity models, both of which are modeled with the aid of the Standish and Yu

and Chang and Deng porosity models. Through numerical modeling of the G3P3 20 kW_t prototype heat exchanger at working temperatures (290-500 °C), either thermal conductivity model will be validated through monodisperse particle distribution simulations. With a thermal conductivity validated, binary particle mixtures will then be explored as the heat transfer media in the G3P3 20 kW_t prototype heat exchanger and optimal bimodal particle distributions in CARBOBEAD HSP and CP will be identified. Identifying these superiorly thermally conductive binary particle mixtures is an important step that could potentially play a critical role in the CSP industry and the current push to develop the world's first 1 MW_t heat exchanger under the Gen3 Particle Pilot Plant (G3P3) program.

CHAPTER TWO: PARTICLE CHARACTERIZATION

2.1 Material Selection and Experimental Methods

Selecting the appropriate heat transfer media is crucial in obtaining optimal performance in a solar thermal facility. For this reason, promising heat transfer media is explored in this section.

2.1.1 Material Selection and Classification

CARBOBEAB HSP 16/30 – 40/70 particle mixtures were the focus of this study. HSP particles are a product of CARBOBEAD, a company that manufactures high-strength ceramic particles traditionally used as fracking proppants in the oil and gas industry. While not as cost effective of a heat transfer material as sand and other readily available and cheap granular materials, CARBOBEAD products perform well from a thermal conductivity standpoint [28], [29]. The size distributions for these particles are listed in CARBOBEAD's particle data sheet [28]. A previous study of CARBOBEAD's particles concluded that there is no significant difference in the particle size when comparing the company's in-house measurements to optical microscopy measurements of the study [30]. Moreover, Christen et al. [23] confirmed this when the researchers used sieves to examine monodispersed and binary mixtures of HSP CARBOBEAD particles. HSP binary particle distributions have been evaluated only at temperatures below 300 °C [23]. At these temperatures, binary HSP particle mixtures demonstrated superior thermal conductivity at ambient temperatures when compared to monodispersed particle distributions at the same temperature.

To classify a binary system, a parameter known as the large particle volume fraction, X_L, is used to clarify the relative amount of the larger particle in the mixture. It should be noted that when X_L is equal to either 0 or 1, that signifies that either 0% or 100% of the

particle distribution is composed of the large particles and it is therefore a monodisperse particle distribution. In order to calculate the size distribution of a binary particle mixture, the following is utilized [23]:

$$Q_{i,binary} = X_L Q_{i,L} + (1 - X_L) Q_{i,s} \quad (1)$$

where $Q_{i,L}$ is the volume fraction of the coarse component, $Q_{i,s}$ is the volume fraction of the fine component, and X_L is the large particle volume fraction. The particle size distribution, particle size ratio, particle density, Sauter mean diameter [31], and average measured diameter for each particle sample used in this study can be found in Table 1.

The Sauter mean diameter [31] is an important measurement method for binary particle distributions and is used in different porosity and thermal conductivity models in this study. It is calculated as prescribed by Tsotsas and Schlunder [32] for particles with the same shape and thermal conductivity as follows:

$$d_p = \left(\sum_{i=1}^{n} \frac{Q_i}{d_i} \right)^{-1} \quad (2)$$

where Q_i is the volume fraction of the particle for a given sieve size, and d_i is the mean particle diameter of a given bin.

Table 2.1 Particles tested in this study. Particle properties can be seen in the CARBOBEAD data sheet [28] **with the exception of the measured particle diameters.**

Material	Sauter Mean Diameter [μm]	Measured Average Diameter [μm]	Particle Density, ρ_s [g /cm^3]	Size Ratio, r[-]	Average Variation in ε [%]	Average ε
HSP 40/70	297	320 ±41.8	3.61	N/A	0.65	.443
HSP 16/30 – HSP 40/70, $X_L = 0.50$	455	N/A		0.304	0.35	.383
HSP 16/30 – HSP 40/70, $X_L = 0.625$	517				1.1	.322
HSP 16/30 – HSP 40/70, $X_L = 0.75$	621				1.23	.39
HSP 16/30	977	865 ±111		N/A	0.62	.43

2.1.2 Porosity Measurement Methods

A driving factor in determining the thermal conductivity in a multigranular packed bed of particles is porosity [32]. Lower size ratios (r, which is also equivalent to the Sauter mean diameter of the fine and coarse components d_s/d_L) also result in a lower porosity [24]. The porosity can be determined by measuring the mass of particles in a known volume with the following formula [23]:

$$\varepsilon = 1 - \frac{m_b}{m_s} = 1 - \frac{m_b}{\rho_s \cancel{V}} \tag{3}$$

where m_b is the bulk mass recorded by the scale and m_s is the mass that would occupy the known volume V if it were non-porous. Calculation of the non-porous mass can be carried out with a knowledge of the absolute density of the particles and the volume that they occupy in the test. In this study, a measured mass of particles taken with a Mettler Toledo XS403S scale was poured into a 100 mL graduated cylinder. The volume occupied by the known mass of particles was recorded and the porosity was calculated using equation (6). This was done 10 times for each large particle volume fraction. The results can be viewed in Table 2.1.

2.1.3 Thermal Conductivity Measurement Methods

In order to measure the thermal conductivity of particle distributions at high temperatures, the Hot Disk TPS 2500 S instrument was employed. The instrument utilizes a transient plane source (TPS) method with a sensor embedded within a sample to calculate thermal conductivity in accordance with ISO22007-2.2 and has a reported error of no more than 5%. The Hot Disk works by utilizing a sensor that consists of an electrically conducting pattern in the shape of a double spiral that is etched into a thin sheet of nickel which is chosen for its well-known temperature coefficient of resistivity [19]. This nickel pattern is laminated between two layers of electrically insulating material composed of Kapton or Mica. The Hot Disk acts as both a heat source for increasing the temperature of a sample and as a ‘resistance thermometer‘ to record the time-dependent temperature increase. A photograph adopted from Hot Disk’s User Manual [19] can be viewed in Figure 2.1.

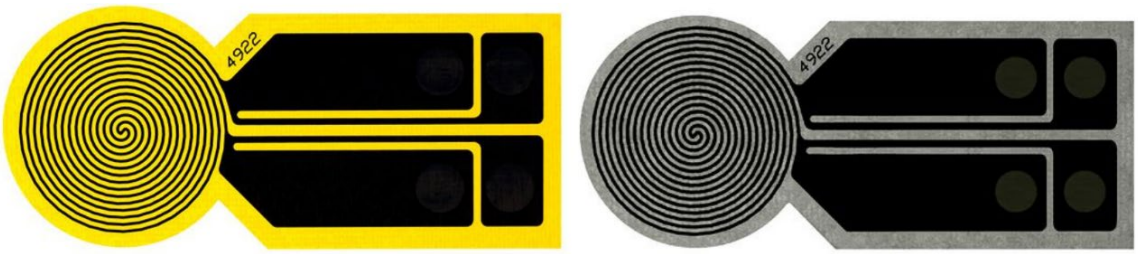

Figure 2.1 A Kapton (left) and Mica (right) Hot Disk sensor. Adopted from [19]**.**

A critical input parameter for the Hot Disk user is the sample Measurement Time. The thermal conductivity of a sample is calculated with the assumption that the sensor is embedded within an infinite amount of the material. This phenomenon can be replicated when a sensor is embedded within a sample of finite volume, however, valid results are bounded by the measurement time. Longer measurement times risk the possibility that the heat wave generated by the sensor that propagates spherically through the material will

contact the boundary or the apparatus confining the sample and skew the results. To prevent invalid results, an appropriate measurement time is a media dependent parameter. Figure 2.1 illustrates a heat wave propagating from the sensor to the boundary surface housing the sample.

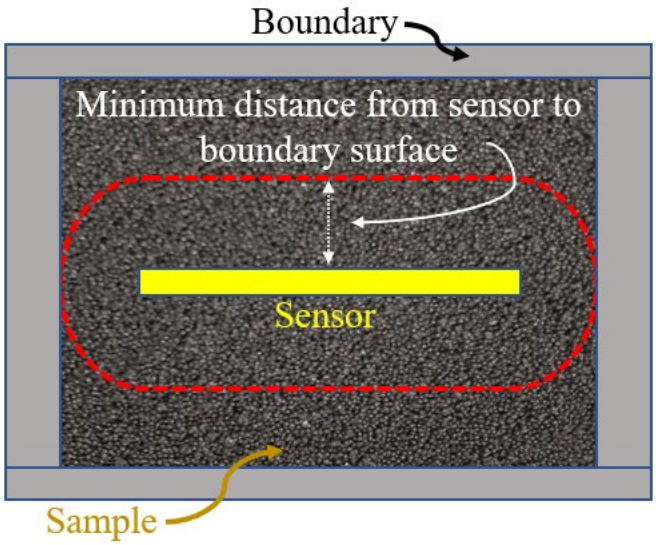

Figure 2.2 Cross sectional view of a sensor embedded within a sample. The white-dotted line represents the maximum distance that the heat wave generated by the sensor can propagate through the sample before contacting the boundary surface illustrated by the red-dotted line. An appropriate measurement time will avoid contacting the boundary surface and yield valid results.

The Hot Disk is electrically heated and therefore the resistance increases as a function of time that can be expressed as the following equation [19]:

$$R(t) = R_0\{1 + \alpha \cdot \{\Delta T_i + \Delta T_{ave}(\tau)\}\} \quad (4)$$

where R_0 is the resistance of the disk right before it is heated at time t = 0, α is the Temperature Coefficient of the Resistivity (TCR), ΔT_i is the constant temperature difference that develops over the thin insulating layers covering both sides of the Hot Disk material and which comprise of the sensor itself. $\Delta T_{ave}(\tau)$ is the temperature increase of the sample

surface on the other side of the insulating layer facing the Hot Disk sensor. Equation (6) can be rearranged to find the temperature increase recorded by the sensor [19]:

$$\Delta T_{ave}(\tau) + \Delta T_i = \frac{1}{\alpha} \cdot \left(\frac{R(t)}{R_0} - 1\right) \tag{5}$$

Throughout the course of a Hot Disk test, electrical resistance heats not only the sensor but the sample as well. The interface of the sample and the sensor at which this temperature is measured is time-dependent and is given by theory [19]:

$$\Delta T_{ave}(\tau) = \frac{P_0}{\pi^{3/2} \cdot a \cdot \Lambda} \cdot D(\tau) \tag{6}$$

where P_0 is the total output power from the sensor, a is the overall radius of the sensor, Λ is the thermal conductivity of the sample being analyzed and $D(\tau)$ is the dimensionless time dependent function represented by

$$D(\tau) = \sqrt{\frac{t}{\Theta}} \tag{7}$$

where *t* is the time that is measured from the start of the transient recording. In equation (7), Θ is the characteristic time, defined as

$$\Theta = \frac{a^2}{\kappa} \tag{8}$$

where κ is the thermal diffusivity of the sample. The characteristic time is an important input parameter in the Hot Disk software. For valid tests, Hot Disk instructs that this parameter must be between .33 and 1 [19]. Keeping the characteristic time within limits is critical for valid data yield.

A computational plot of the recorded sample temperatures and $D(\tau)$ yields a straight line; the slope of which can be represented by

$$\frac{P_0}{\pi^{7/2} \cdot a \cdot \Lambda} \tag{9}$$

When testing a new sample, both Θ and κ are unknown. The slope of the line represented in equation (9) and an iterative process are imposed in order to find both Λ and κ. Therefore, from a single transient recording (or a single Hot Disk test) the thermal conductivity of a sample can be calculated [19].

The heat induced into the sample by way of the Hot Disk sensor is evident in an ambient temperature thermal conductivity convergence test with HSP 16/30-40/70 particles at $X_L = .625$. The results of this convergence test can be viewed in Figure 2.3. In this figure, consecutive tests were carried out on the same sample with varying interval times to allow heat induced by the sensor into the sample to dissipate. A test carried out exactly after the last had been completed resulted in a thermal conductivity error of 11.41%. Waiting at least 25 minutes will reduce this error to .29%. Therefore, a minimum of at least 25 minutes and ideally an hour interval between tests is always implemented so as to allow heat induced into the sample to dissipate.

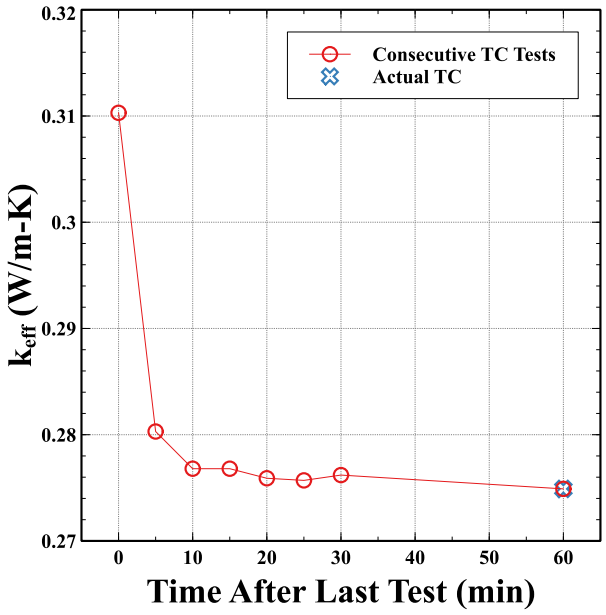

Figure 2.3 Ambient temperature thermal conductivity convergence test for HSP 16/30-40/70 particles at $X_L = .625$.

For temperatures ranging from 0 to 300 °C, an F1 5501 Kapton sensor with a diameter of 6.4 mm was utilized with a Hot Disk Standard Gray Cable. Embedding the Kapton sensor within particles involves filling the bottom chamber with particles, concentrically mounting the Kapton sensor on top of the particles and then placing the top chamber on before also filling it with particles. This process is illustrated in Figure 2.4.

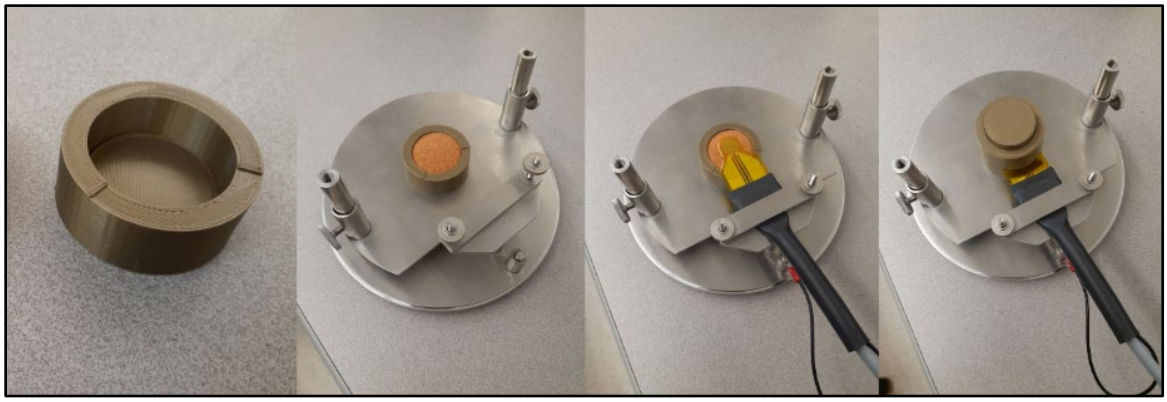

Figure 2.4 Process of loading the testing chamber with particles and embedding an F1 5501 Kapton sensor. The sensor shown is connected to the Hot Disk TPS 2500 S via a Standard Gray Cable.

For temperatures above 300 °C, an F1 4901 mica sensor with a diameter of 9.7 mm and a PEEK High Temperature Cable is utilized. In order to embed the sensor within a particle distribution, a stainless-steel particle chamber with an inner diameter of 22 mm is employed. This chamber is housed inside a Thermolyne FB1415 Benchtop Muffle Furnace. The chamber is composed of a top and bottom, both with a height of 20 mm. Particles are poured into the bottom portion of the chamber until the bottom portion is filled. The sensor is embedded within the particles in the same way as before. After embedment, the muffle furnace is then closed and heated to the desired temperature as can be seen in Figure 2.5. Once the sample has reached steady state, a thermal conductivity test can be executed

through the Hot Disk software.

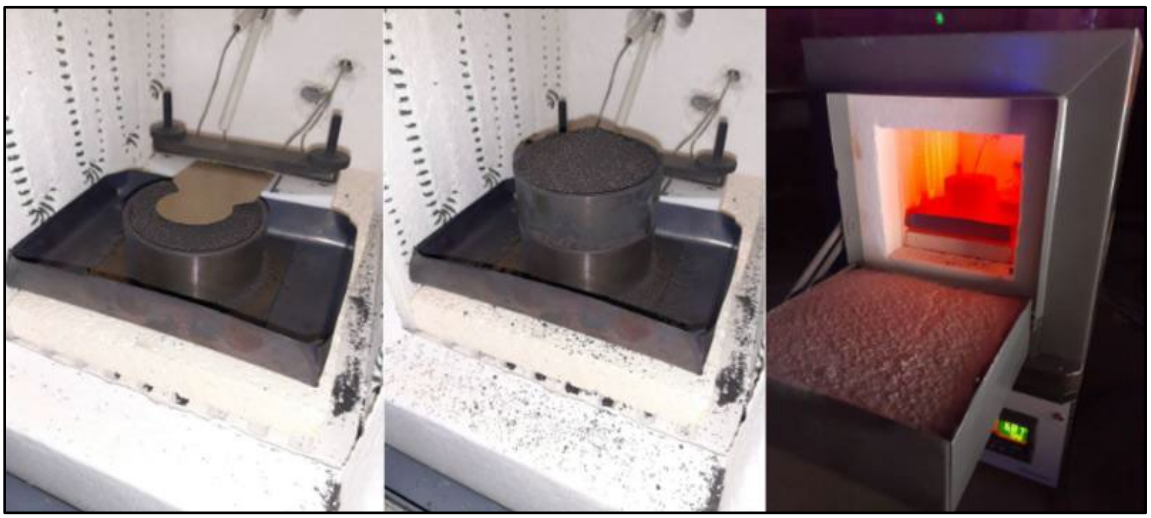

Figure 2.5 Process of loading the stainless-steel testing chamber with particles and embedding an F1 4901 Mica sensor. The sensor is connected to the Hot Disk TPS 2500 S via a PEEK High-Temperature cable. The apparatus is housed within a Thermolyne FB1415 Benchtop Muffle Furnace for high-temperature testing.

2.1.4 Thermal Conductivity Under Load Measurement Methods

To measure the thermal conductivity of HSP CARBOBEAD particles under load, particles are placed within a testing chamber and a Kapton sensor is embedded within the particles. A cross sectional diagram of this setup can be viewed in Figure 2.6 and the actual setup can be seen in Figure 2.7. A Hot Disk Kapton F1 5051 sensor is utilized as only ambient temperatures are employed.

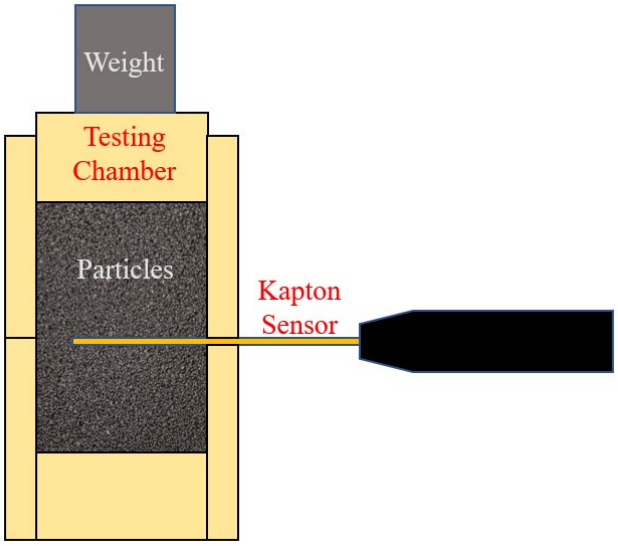

Figure 2.6 Cross sectional view of Kapton sensor embedded within particles under load.

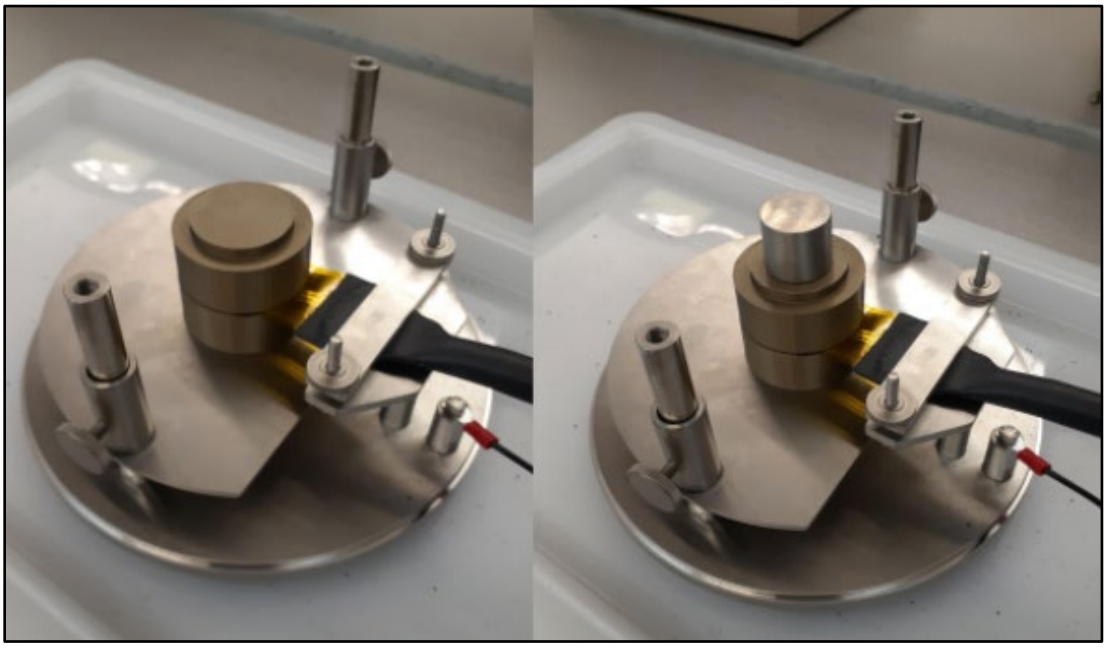

Figure 2.7 Experimental setup for particle thermal conductivity testing under load with the 5051 Kapton sensor and the Hot Disk TPS 2500 S.

Once particles have been placed within the testing chamber and the sensor has been embedded, a weight of known mass can be placed on top of the testing chamber. Special care is taken to not tamp the particles when placing the weight as this would dramatically reduce the porosity of the particle distribution and yield an inaccurate thermal conductivity reading for the given particle distribution.

2.1.5 Methodology to Account for Variation in Particle Packing Structure

Particle packing structure plays an important role in determining the thermal conductivity of a particle distribution. It is inevitable that the packing structure will change when particles are removed from the testing chamber and are again replaced with even the same particles. This change in packing structure directly influences the porosity of the particle distribution. For this reason, great care is taken when performing measurements so as to pour particles into the testing chamber in the same manner each time and to not cause vibrations that increase packing density. Even with these precautions, variation in thermal conductivity readings occur. For this reason, differentiation between two types of tests must be explicitly defined: fresh and stale pours. The former refers to particles being replaced after each measurement and the latter refers to particles not replaced after each measurement. Stale pours lead to better characterization of different particle distributions, but are drastically more time consuming, ultimately resulting in higher error percentages due to the limited number of tests. Tests are carried out until data complies with Georgia Tech's Measurement Acceptability Criteria for heat transfer media requiring an error no more than 15% across all tests [33]. This usually requires about 4-5 freshly poured particle tests for each particle distribution at each temperature.

2.1.6 Error Propagation and Measurement Acceptability Criteria

An important aspect of any routine data collection is accounting for the propagation of error. Correctly capturing properties similar to thermal conductivity at high temperatures requires a rigorous error propagation methodology. The work in this study adheres to the standards set forth by Georgia Tech's Uncertainty Analysis and Error Propagation Methodology for Reporting Thermophysical Properties and Measurements of Gen3 CSP Materials [34]. Utilizing a 95% confidence interval, k', or the best estimate of a sample's thermal conductivity, can be written as

$$k' = \bar{k} \pm u_k \tag{10}$$

where $\bar{k}$ is the mean thermal conductivity value and u_k is the uncertainty in the mean thermal conductivity value. The uncertainty in the mean thermal conductivity value can be expanded as follows:

$$u_k = t_{v_k,95}\sqrt{b_{\bar{k}}^2 + s_{\bar{k}}^2} \tag{11}$$

where $t_{v_k,95}$ is the appropriate *t* value from the Student's *t* Distribution Table for a 95% confidence interval and v_k is the degrees of freedom in the *k* calculation which is equal to the number of measurements, *M*. $b_{\bar{k}}$ and $s_{\bar{k}}$ are the systematic and random standard and uncertainties, respectively. Hot Disk claims that the hardware is capable of determining the thermal conductivity of a sample with an error of no more than ±5%. This systematic error can be expressed as

$$(b_{\bar{k}}) = \left(\frac{5\% \times \langle \bar{k} \rangle}{2}\right) \tag{12}$$

The random standard uncertainty can be expressed as

$$(s_{\bar{k}})_2 = \frac{s_k}{\sqrt{M}} \tag{13}$$

where s_k is the standard deviation of the thermal conductivity measurements defined as

$$s_k = \left[\frac{1}{M-1}\sum_{m=1}^{M}\left(\bar{k}_m - \langle\bar{k}\rangle\right)^2\right]^{1/2} \quad (14)$$

Therefore, a thermal conductivity measurement will have a percentage of uncertainty of as follows:

$$\frac{u_k}{\bar{k}} = \frac{t_{v_k,95}\sqrt{b_{\bar{k}}^2 + s_{\bar{k}}^2}}{\bar{k}} \times 100 \quad (15)$$

Equation (15) must be less than 15% for the measurement to comply with the Measurement Acceptability Criteria (MAC) [34].

2.2 Porosity Modeling

2.2.1 The Standish and Yu Porosity Model

In general terms, the porosity of a monodispersed bed of particles ranges between .36 and .4 depending on density of the packed system [35]. Moreover, this same relationship has shown good agreeance with discrete element method simulations for particles with diameters between 100-1000 μm [36]. Other studies have reported that granular media shows a larger porosity range from .35 to .48 [14]. In many commonly used heat exchanger models, a porosity range or .4-.45 is utilized [11], [37]. For modeling purposes in this study, every particle system will be considered monodispersed with a single particle size calculated with the Sauter mean diameter [31]. Strictly speaking, the CARBOBEAD monodispersed distributions are not perfectly monodispersed as not every particle is not exactly the same size. For this reason, the Sauter mean diameter is useful and is employed for all particle distributions. Two porosity models will be employed in this study to better understand the impact of porosity on the overall heat transfer of a particle distribution.

The Standish and Yu porosity model [24] employs a conic equation that has the ability to generally describe the relationship between the fractional solid volumes of binary mixtures and the specific volume:

$$\left(\frac{V-V_1X_1}{V_2}\right)^2 + 2G\left(\frac{V-V_1X_1}{V_2}\right)\left(\frac{V-X_1-V_2X_2}{V_1-1}\right) + \left(\frac{V-X_1-V_2X_2}{V_1-1}\right)^2 = 1 \tag{16}$$

where V is the specific volume of the binary packing, V_1 & V_2 are the partial specific volumes of the particles in the mixture and X_1 and X_2 are the solid volume fractions of the coarse and fine particles. G is a parameter dependent on the initial specific volumes and the size ratio. It should be noted that X_2 = 1 - X_1. V can be expressed in the following form:

$$V = \frac{-B+\sqrt{B^2-4AC}}{2A} \tag{17}$$

where

$$A = \left(\frac{1}{V_2}\right)^2 + \frac{2G}{V_2(V_1-1)} + \frac{1}{(V_1-1)^2} \tag{18}$$

$$B = -\frac{2V_1X_1}{(V_2)^2} + \frac{2G}{V_2(V_1-1)}(V_2X_1 - V_2 - X_1 - V_1X_1) + \frac{2(V_2X_1-V_2-X_1)}{(V_1-1)^2} \tag{19}$$

$$C = \left(\frac{V_1X_1}{V_2}\right)^2 - \frac{2G}{V_2(V_1-1)}V_1X_1(V_2X_1-V_2-X_1) + \left(\frac{(V_2X_1-V_2-X_1)^2}{(V_1-1)^2}\right) - 1 \tag{20}$$

The maximum void contraction $\Delta\epsilon(r)$ and the corresponding solid volume X_1^{max} can be calculated with the following equations:

$$\Delta\epsilon(r) = \begin{cases} \epsilon^0(1-\epsilon^0)(1-2.35r+1.35r^2) & r \leqslant 0.741 \\ 0 & r > 0.741 \end{cases} \tag{21}$$

$$X_1^{max} = \frac{1-r^2}{1+\epsilon^\circ} \tag{22}$$

where r is the size ratio of the two particles in the binary mixture and ϵ^0 is the void contraction (or initial porosity) of a particle mixture which can simply be calculated experimentally by taking the average of each of the bulk porosities of the particles in a binary particle mixture. X_1^{max} will correspond to the large particle volume fraction that will lead to the lowest porosity.

The assumption that the binary mixtures experience a maximum void contraction, the minimum specific volume V_{min} of the binary mixture and the previously unknown parameter G can then be expressed as follows:

$$V_{min} = \frac{1}{1-\varepsilon_0+\Delta\varepsilon(r)} \tag{23}$$

$$G = \frac{1-\left(\frac{V_{min}-V_1X_1^{max}}{V_2}\right)^2-\left(\frac{V_{min}-V_2-X_1^{max}+V_2X_1^{max}}{V_{1-1}}\right)^2}{2\left(\frac{V_{min}-V_1X_1^{max}}{V_2}\right)\left(\frac{V_{min}-V_2-X_1^{max}+V_2X_1^{max}}{V_{1-1}}\right)} \tag{24}$$

Upon successful calculation of the parameter G and the specific volume V of the binary mixture, the packing density ϕ can then be calculated by

$$\phi = \frac{1}{V} \tag{25}$$

Finally, the packed bed porosity can then be determined with

$$e = 1 - \phi \tag{26}$$

The Standish and Yu porosity model is an extremely important tool in visualizing the porosity of many size ratios and large particle volume fractions as can be seen in Figure 2.8. According to the figure, the optimal porosity for the HSP 16/30-40/70 particle mixture can be obtained when X_L = .575-.6.

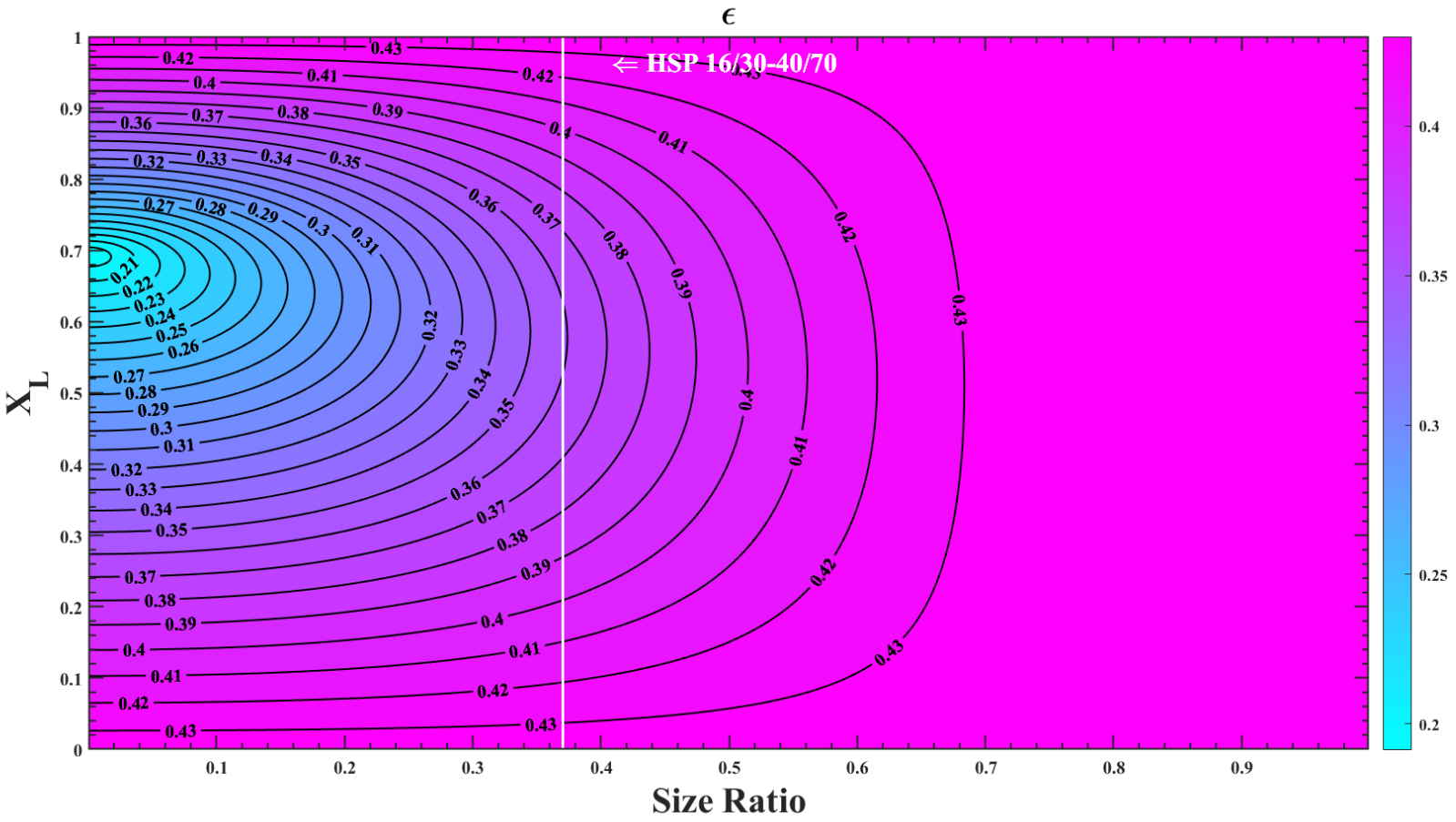

Figure 2.8 The Standish and Yu Porosity Model imposed on different size ratios and large particle volume fractions. The large particle in each mixture is the HSP 16/30 particle. The HSP 16/30-40/70 particle mixture is represented with a vertical white line.

2.2.2 The Chang and Deng Porosity Model

While the Standish and Yu porosity model provides a linear solution, the Chang and Deng porosity model provides a non-linear solution that has shown increased accuracy for particle mixtures of multiple sizes [25]. The procedure operates on the basis of two potential porosity values that can be calculated as follows:

$$\varepsilon^{(1)} = \varepsilon_1 X_1 + \left(\varepsilon_2 - a_2^{(1)}(1+\varepsilon_2)\right) X_2 \tag{27}$$

$$\varepsilon^{(2)} = \left(\varepsilon_1 - b_1^{(2)}(\varepsilon_1)\right) X_1 + \varepsilon_2 X_2 \tag{28}$$

where ε_1 and ε_2 are the experimentally measured bulk porosities of the small and large particles respectively. The filling mechanism coefficient a_j and the embedment mechanism coefficient b_j are functions of the particle size ratio and can be determined from the following equations:

$$a_j^{(i)} = \left(1 - \frac{d_j}{d_i}\right)^p \quad for\ \ d_i > d_j\ (0\ for\ d_j \geq d_i) \tag{29}$$

$$b_j^{(i)} = \left(1 - \frac{d_i}{d_j}\right)^s \quad for\ \ d_i < d_j\ (0\ for\ d_i \geq d_j) \tag{30}$$

where d_i and d_j are the particle diameters of the ^{ith} and ^{jth} particles respectively. The variables p and s are empirically determined constants.

Parameters p and s can be determined empirically by utilizing experimentally measured porosity values at various large particle volume fractions. Once various values of X_L have been plotted, the slopes at each end of the curve need be calculated. Consider the variable y_1 and y_2 representing the solid volume fraction of the particles in a binary mixture. Taking into account the slopes on either end of the curve generated by the experimental data, two equations need be utilized:

$$e = e_1 y_1 + \big(e_2 - a(1 + e_2)\big) y_2 \tag{31}$$

$$e = e_2 y_2 + (e_1 - b e_1) y_1 \tag{32}$$

Similar to the equations for the filling mechanism coefficient a_j and the embedment mechanism coefficient b_j, definite values can be determined for these variables with the following:

$$a = \left(1 - \frac{d_2}{d_1}\right)^p \tag{33}$$

$$b = \left(1 - \frac{d_2}{d_1}\right)^s \tag{34}$$

Then, taking the derivative of equations (33) and (34), the relationship to the slopes of either side of the experimental data curve is introduced as the terms $\left(\frac{de}{dy_2}\right)$ in both the following equations representing each respective slope:

$$a = \frac{e_2 - e_1}{1 + e_2} - \frac{1}{1 + e_2}\left(\frac{de}{dy_2}\right) \tag{35}$$

$$b = \frac{1}{e_1}\left(\frac{de}{dy_2}\right) - \frac{e_2 - e_1}{e_1} \tag{36}$$

The slopes of $\left(\frac{de}{dy_2}\right)$ can easily be determined from the experimental data and then the parameters of *p* and *s* can be calibrated. In-depth detail of this procedure can be found in the appendix of Chang and Deng's work [25]. After the two potential porosity values are found, the porosity of the mixture can be determined as the maximum porosity of the values obtained for each class of particles:

$$\varepsilon = max\big(\varepsilon^{(1)}, \varepsilon^{(2)}\big) \tag{37}$$

Fitting parameters utilized in the Chang and Deng porosity model for CARBOBEAD HSP particles can be found in Table 2.2. Unlike the Standish and Yu porosity model, the Change and Deng porosity model relies on experimental data for each

particle mixture it is imposed on. Therefore, full-scale porosity modeling such as that found in Figure 2.8 is not possible as the parameters *p* and *s* would need to be calibrated based on experimental data for each and every size ratio.

Table 2.2 Fitting parameters used for the Chang and Deng porosity model.

Particle Type	d_1 [μm]	d_2 [μm]	e_1	e_2	a	b	p	s
HSP	866	321	.386	.382	.0579	.2487	6.15	3

2.3 Thermal Conductivity Modeling

2.3.1 The Zehner, Bauer and Schlunder (ZBS) Thermal Conductivity Model

The ZBS model [38] is widely used and employed in this study to calculate the bulk effective packed-bed thermal conductivity [26] and can be expressed as follows:

$$\frac{k_{s,eff}}{k_f} = \left(1-\sqrt{1-\varepsilon}\right)\varepsilon\left[\left(\varepsilon - 1 + \frac{1}{\kappa_G}\right)^{-1} + \kappa_r\right] + \sqrt{1-\varepsilon}[\varphi\kappa + (1-\varphi)k_c] \quad (38)$$

where k_f is the gas thermal conductivity, ε is the packed bed porosity, κ_G is the gas conduction ratio in the Knudsen regime, κ_r is the radiation ratio parameter, κ is a dimensionless parameter, k_c is a conduction term, and φ is the empirical contact parameter. Here, k_c can be expressed as follows:

$$k_c = \frac{2}{N}\left\{\frac{B(\kappa+\kappa_r-1)}{N^2\kappa_G\kappa}\ln\frac{\kappa+\kappa_r}{B[\kappa_G+(1-\kappa_G)(\kappa+\kappa_r)]} + \frac{B+1}{2B}\left[\frac{\kappa_r}{\kappa_G} - B\left(1+\frac{1-\kappa_G}{\kappa_G}\kappa_r\right)\right] - \frac{B-1}{N\kappa_G}\right\} \quad (39)$$

where *B* is the deformation parameter. A more accurate value for the deformation parameter is provided by Hsu et al. [39] and can be found below:

$$B = 1.364\left(\frac{1-\varepsilon}{\varepsilon}\right)^{1.055} \quad (40)$$

The parameter *N* is represented as follows:

$$N = \frac{1}{\kappa_G}\left(1+\frac{\kappa_r - B\kappa_G}{\kappa}\right) - B\left(\frac{1}{\kappa_G}-1\right)\left(1+\frac{\kappa_r}{\kappa}\right) \quad (41)$$

It then follows that κ_r and κ_G can be represented by the following:

$$\kappa_r = \frac{k_e^r}{k_f} = \frac{4\sigma}{\left(\frac{2}{\varepsilon_r}-1\right)} T^3 \frac{d_p}{k_f} \tag{42}$$

$$\kappa_G = \frac{k_G}{k_f} = \left[1 + \left(\frac{l}{d_p}\right)\right]^{-1} \tag{43}$$

Here, k_e^r is the thermal radiative conductivity, k_f is the molecular thermal conductivity of the gas outside the Knudsen regime, σ is the Stephon-Boltzmann constant and l is the modified free path of gas molecules defined by

$$l = 2\frac{2-a_T}{a_T}\left(\frac{2\pi\tilde{R}T}{M_g}\right)^{1/2} \cdot \frac{k_f}{P\left(2C_p - \tilde{R}/M_g\right)} \tag{44}$$

where a_T is the thermal accommodation coefficient, $\tilde{R}$ is the universal gas constant, C_p is the specific heat at constant pressure and M_g is the molecular mass of the gas. a_T is then defined as

$$a_T = \exp\left[-0.57\left(\frac{T_S - T_0}{T_0}\right)\right]\left(\frac{M^*}{6.8+M^*}\right) + \frac{2.4\mu}{(1+\mu)^2}\left\{1 - \exp\left[-0.57\left(\frac{T_S - T_0}{T_0}\right)\right]\right\} \tag{45}$$

where $\mu = M_g/M_s$ is the ratio between the molecular masses of the gases, the solid surface and

$$M^* = \begin{cases} M_g \text{ for monoatomic gases} \\ 1.4M_g \text{ for diatomic/polyatomic gases} \end{cases} \tag{46}$$

The ZBS has been employed in numerous studies [11], [14], [40], [41] and current literature concerning shell-and-plate moving packed-bed heat exchangers and applies to monodispersed particle distributions at a constant porosity [10]. The work of Christen et al. demonstrated the ability of the ZBS model to adequately model data in conjunction with either aforementioned porosity model and that it could be effectively utilized at higher temperatures [23].

The ZBS model has many input parameters including packed-bed porosity (ε), packed bed temperature (T), particle diameter (d_p), particle emissivity (ε_r), an empirical particle contact parameter (ϕ), the solid particle thermal conductivity (k_s), gas thermal conductivity (k_f) and gas pressure (P). The ZBS model parameters utilized with their associated references can be found in Table 2.3.

The initial porosity values for the HSP binary particle mixtures evaluated in this study were calculated by taking the average porosity value across 10 trials resulting in .43 for HSP 16/30 and .443 for HSP 40/70 as can be seen in Table 2.1. It should be noted that the accepted porosity values for loose and densely packed spheres are .4 and .36, respectively [35]. However, the particles used in this study are not perfectly spherical and therefore higher recorded levels of porosity are expected. Furthermore, Albrecht and Ho use an initial porosity of .45 in their shell-and-plate heat exchanger modeling efforts [11].

Table 2.3 Parameters and assumptions for the ZBS thermal conductivity model.

Property	Symbol	Value	Units	Ref.
Particle Diameter	d_p	5 - 866	μm	-
Initial Porosity	ε	0.45	-	[42]
Particle Emissivity	ε_r	0.9	-	[8]
Empirical Particle Contact	ϕ	0.01	-	[43]
Solid Particle Thermal Conductivity	k_s	2.0	W/m-K	[10]
Gas Thermal Conductivity	k_f	Air(T)	W/m-K	[44]
Pressure	P	101.325	kPa	-

2.3.2 The Yagi and Kunii Thermal Conductivity Model

A slightly older but efficient thermal conductivity model is that of Yagi and Kunii [27]. While not as widely used as the ZBS model, it still has been employed in catalytic packed particle bed reactors of methanol [45], heat transfer in ash deposits of utility boilers [46] and pyrolysis fixed bed reactors [47]. Furthermore, it has also been employed

in particle-to-sCO_2 heat exchangers [18]. The Yagi and Kunii model defines the effective thermal conductivity as

$$\frac{k_e^\circ}{k_g} = \frac{\beta(1-\epsilon)}{\gamma\left(\frac{k_g}{k_s}\right)+\frac{1}{(1/\varphi)+(D_p h_{rs}/k_g)}} + \epsilon\beta\frac{D_p h_{rv}}{k_g} \quad (47)$$

where β and γ are constants (traditionally, both of value 1 for packed particle bed practical purposes), k_e° is the effective thermal conductivity of a packed-bed with motionless fluid, ϵ is the porosity of the particle distribution, k_g is the motionless fluid thermal conductivity, k_s is the solid particle thermal conductivity, D_p is the particle diameter, h_{rs} is the heat transfer coefficient of thermal radiation from solid surface to solid surface and h_{rv} is the heat transfer coefficient of thermal radiation from void to void. h_{rs} and h_{rv} can be expressed as follows:

$$h_{rs} = 0.1952\left(\frac{\varepsilon_r}{2-\varepsilon_r}\right)\left(\frac{T_s}{100}\right)^3 \quad (48)$$

$$h_{rv} = \frac{0.1952}{1+\left(\frac{\varepsilon}{2(1-\varepsilon)}\right)\left(\frac{1-\varepsilon_r}{\varepsilon_r}\right)}\left(\frac{T_s}{100}\right)^3 \quad (49)$$

where ε_r is the solid particle emissivity and T_s is the solid particle temperature (K).

All these aforementioned parameters can be found in detail Yagi and Kunii's work [27]. The parameter ϕ can be found from

$$\phi = \frac{1}{4}\left(\frac{\{(K-1)/K\}^2}{ln\,K-(K-1)/K}\right) - \frac{1}{3K} \quad (50)$$

where K is the ratio of the particle to the gas phase thermal conductivity [48].

2.4 Thermal Conductivity Experimental Results

2.4.1 HSP Ambient Temperature Thermal Conductivity Results

Ambient temperature testing of particles primarily illustrates the heat transfer mechanisms of convection and conduction as radiation is more prominent at higher

temperatures [11]. Therefore, as conduction is a primary vehicle of heat transfer at ambient temperatures, it would be expected that less porous media would constitute higher thermal conductivities. This is evident in Figure 2.9 where when the porosity is lower, the thermal conductivity is higher. It can be concluded that at lower temperatures, particle distributions with the lowest porosity will yield the highest thermal conductivities. In this manner, particle distributions with X_L = .5-.75 are optimal as they boast decreased porosity and increased thermal conductivity. Recall Figure 2.8 where the Standish and Yu porosity model was imposed on the HSP 16/30-40/70 particle mixture. Figure 2.8 projected that the optimal large particle volume fraction for the HSP 16/30-40/70 particle mixture was around .6. This projection can be validated with the experimental porosity data found in Figure 2.9.

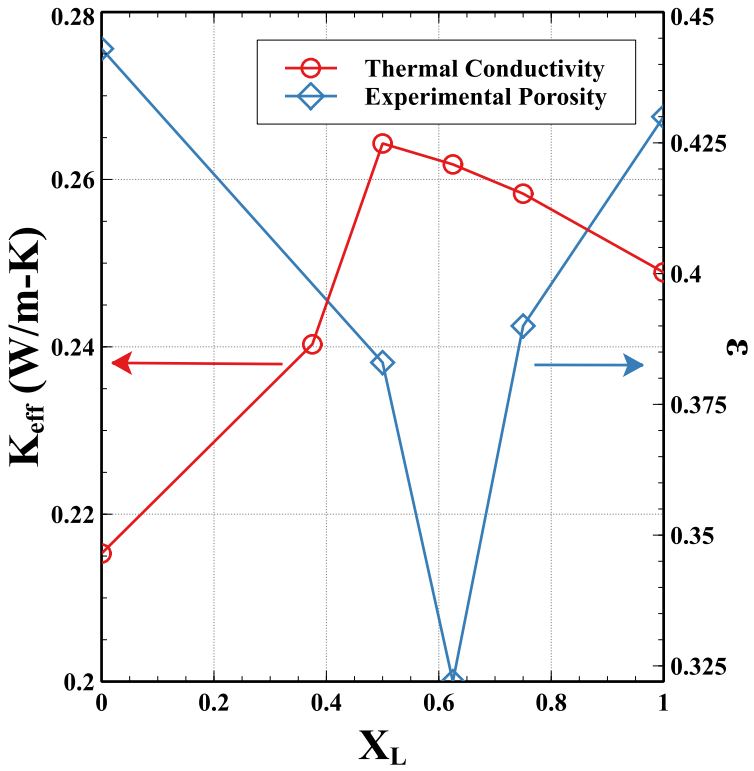

Figure 2.9 Ambient temperature thermal conductivity and experimental porosity for HSP 16/30-40/70 particles.

2.4.2 HSP Ambient Temperature Thermal Conductivity Results Under Load

Imposing a load upon a powdered substance has shown to increase thermal conductivity in an asymptotic manner [19]. This was also found to be the case with CARBOBEAD's HSP particles that were examined when in a binary particle mixture. As can be seen in Figure 2.10 and 2.11, weight applied to the particles in excess of ~300 g has a diminishing effect on the corresponding thermal conductivity. It is also noteworthy that the highest achieved thermal conductivity for the HSP particles under load is when X_L = .625 and .75. This is due to the reduced porosity that is a product of a binary particle distribution. Recalling Table 2.1, X_L = .625 has the lowest recorded experimental porosity while also boasting the highest thermal conductivity when 700 g of weight was applied. Adversely, monodisperse particle distributions such as pure HSP 16/30 or HSP 40/70 yield significantly lower thermal conductivities due to their relatively higher porosity. All large particle volume fractions increase at a similar rate; however, the binary mixtures, i.e., X_L = .5, .625 and .75 increase several percentage points more than the purely monodispersed particle distributions throughout the loading analysis.

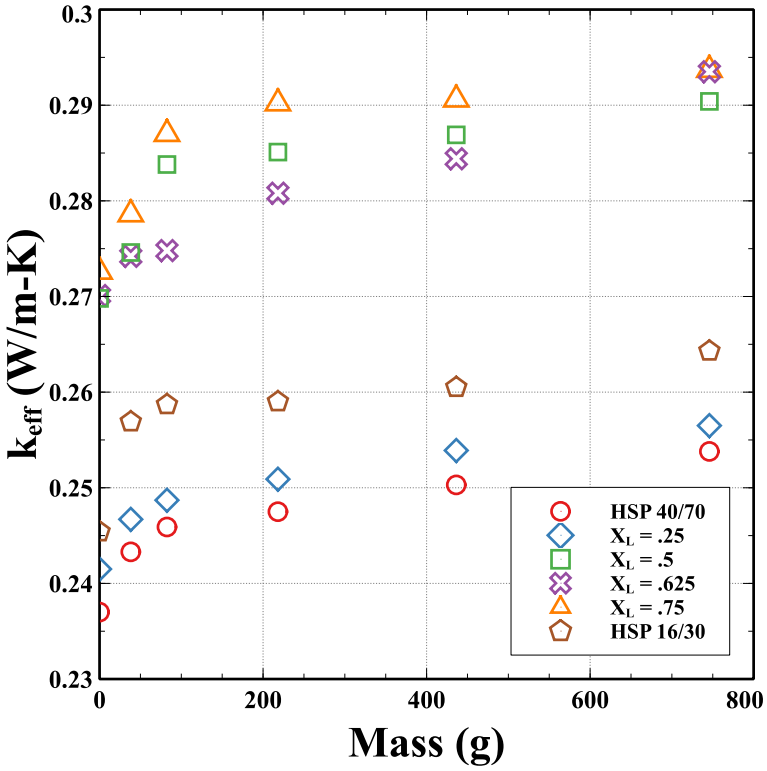

Figure 2.10 Weight vs. effective thermal conductivity for HSP binary particle mixtures evaluated at room temperature. Note that the large particle in this binary mixture is HSP 16/30.

This could yield significant savings in solar thermal facilities that utilize solid particles as thermal energy storage or as heat transfer media. Engineering a mechanism where an on-demand force could be applied could drastically improve efficiencies and operating costs. Relatively small amounts of force applied in an efficient manner could see improvements in thermal conductivities by up to 8-10% as can be verified by Figure 2.11.

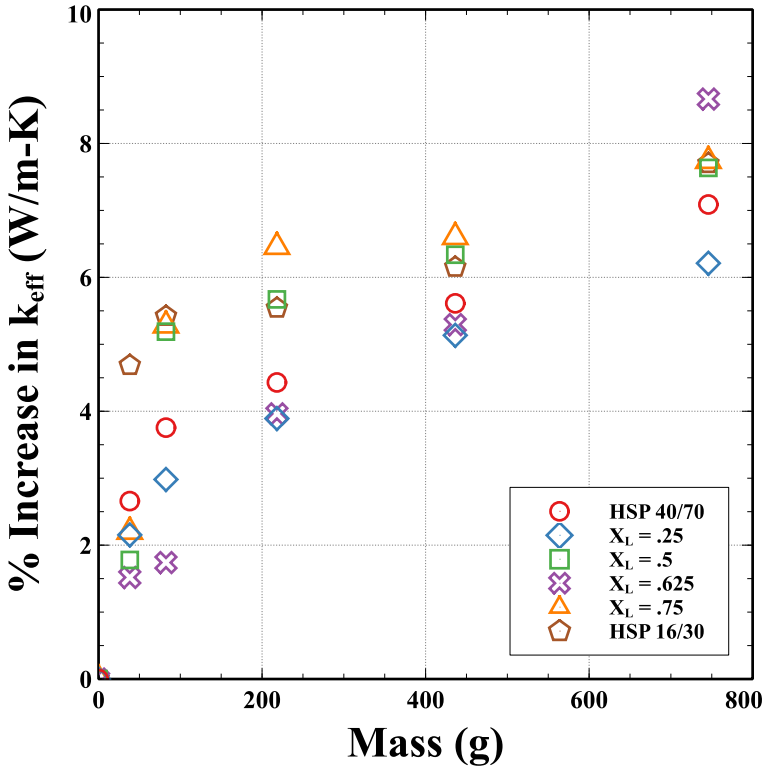

Figure 2.11 Weight vs. the percent increase in effective thermal conductivity for HSP binary particle mixtures evaluated at room temperature. Note that the large particle in this binary mixture is HSP 16/30.

2.4.3 HSP High Temperature Thermal Conductivity Results

It has been established that at temperatures up to 300℃, a binary particle distribution yields superior thermal conductivity when compared to a monodispersed distribution at the same temperature [23]. The high-temperature setup illustrated in Figure 2.5 was validated by comparing HSP 40/70 thermal conductivity tests carried out with a transient hot wire [29]. A graphical comparison is found in Figure 2.12 illustrating the legitimacy of the setup.

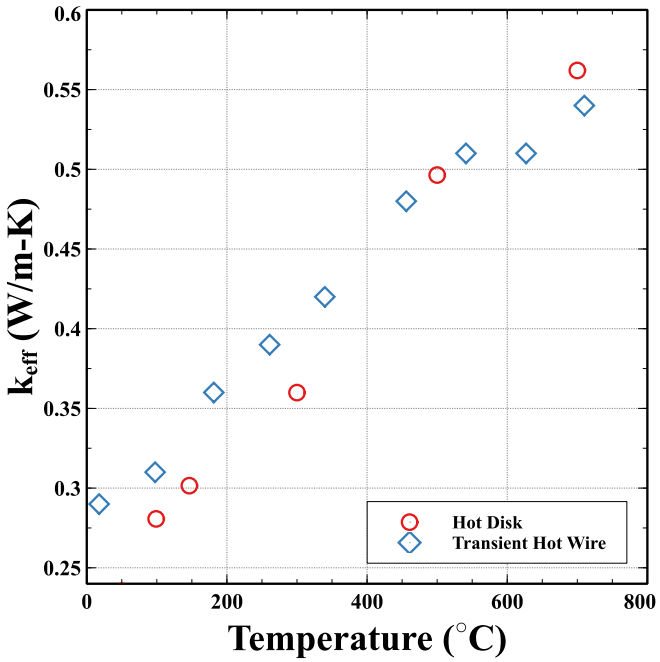

Figure 2.12 Validation of Hot Disk high-temperature setup. CARBOBEAD HSP 40/70 thermal conductivity results at variable temperatures obtained by way of the Hot Disk were compared to the same particles whose data was obtained by way of a transient hot wire [29]**.**

Consider Figure 2.13 and how particle distributions composed purely of larger particles yield the highest thermal conductivities. HSP 16/30 particles perform significantly better than their counterparts at the same temperature. Furthermore, pure HSP 40/70 particles perform the worst at higher temperatures in terms of recorded thermal conductivity. From 300-500 °C, the thermal conductivity of a binary particle distribution is equal to that of a monodispersed distribution composed of the larger particles. Below this temperature, a binary particle mixture would yield superior thermal conductivities. At higher temperatures, monodispersed distributions composed of the larger particles would yield superior thermal conductivities.

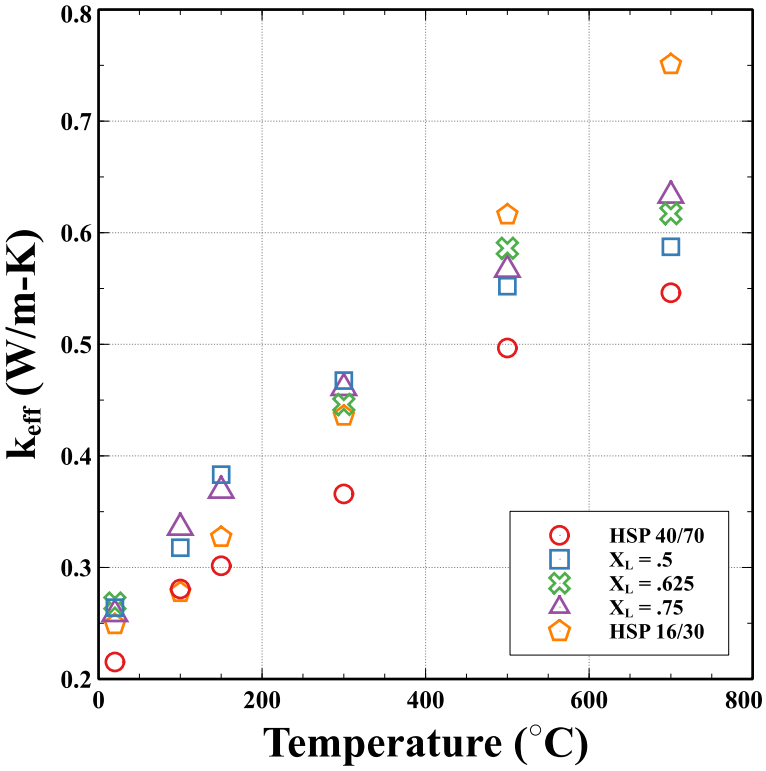

Figure 2.13 Temperature vs. effective thermal conductivity for HSP 16/30-40/70 particle distributions.

This significant increase in the thermal conductivities of large-particle monodispersed distributions is likely due to the enhanced surface radiation of larger particles at higher temperatures. The surface radiation is the dominant heat transfer mechanism at high temperatures and increases exponentially with temperature. The contribution of surface radiation to the effective thermal conductivity increases with particle diameter because the emission from one particle to its adjacent moves a larger distance. In this manner, particles act as "radiative shields" inhibiting the radiation component of heat transfer at higher temperatures [11].

Binary particle distributions employ a number of smaller particles within a mixture. These smaller particles inhibit the radiation of the larger particles across the gap to other larger particles. Consider Figure 2.14 where a cross-sectional view of a binary

particle distribution and a monodispersed distribution composed entirely of larger particles can be examined.

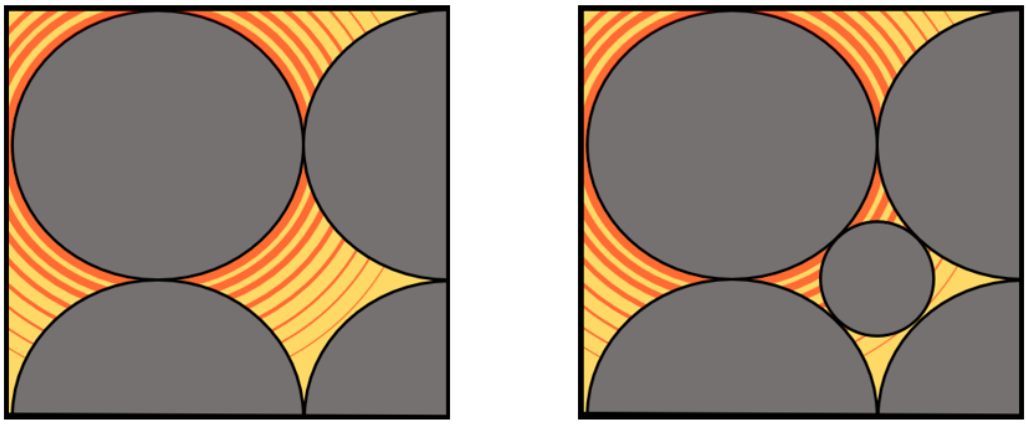

Figure 2.14 Diagrams of a monodispersed particle distribution composed purely of larger particles (left) and a binary particle distribution (right). In the binary particle distribution, the radiative component of heat transfer is inhibited by the smaller particle which acts similar to a "radiative shield" [11].

For the best heat transfer at high temperatures, large particle monodisperse distributions should be utilized. Many moving packed-bed shell-and-plate heat exchangers have particle diameter limitations restricting the potent radiative heat transfer of larger particle diameters at high temperatures. It is optimal to employ the largest particle size possible that does not restrict particle channel flow [7] or hinder the overall heat transfer coefficient.

2.4.4 HSP ZBS Results

The ZBS thermal conductivity model for various temperatures utilizing both the Standish and Yu and the Chang and Deng porosity models is compared to experimental data in Figure 2.15. It is observed that at 21 °C, the ZBS thermal conductivity model with either of the porosity models is an excellent fit for the experimental data set. This is not the case at higher temperatures. While at lower temperatures, the experimental data is parabolic in shape. At higher temperatures the experimental data transitions to a more

exponential shape. The transition between the parabolic and exponential shape of the data happens between 300 and 500 °C. From Figure 2.13 we know that this transition temperature is most likely ~400 °C. Up until about 300 °C, the ZBS thermal conductivity method resembles the shape of the experimental data, albeit it is shifted down compared to the data. This is indicative that above 300 °C the ZBS method is not dependable for accurate thermal conductivity characterization.

Error bars were calculated for the recorded thermal conductivity measurements in Figure 2.15 using a 95% confidence interval, the student's t-test [49] and Georgia Tech's Uncertainty Analysis and Error Propagation Methodology for Reporting Thermophysical Property Measurements of Gen3 CSP Materials procedure [34].

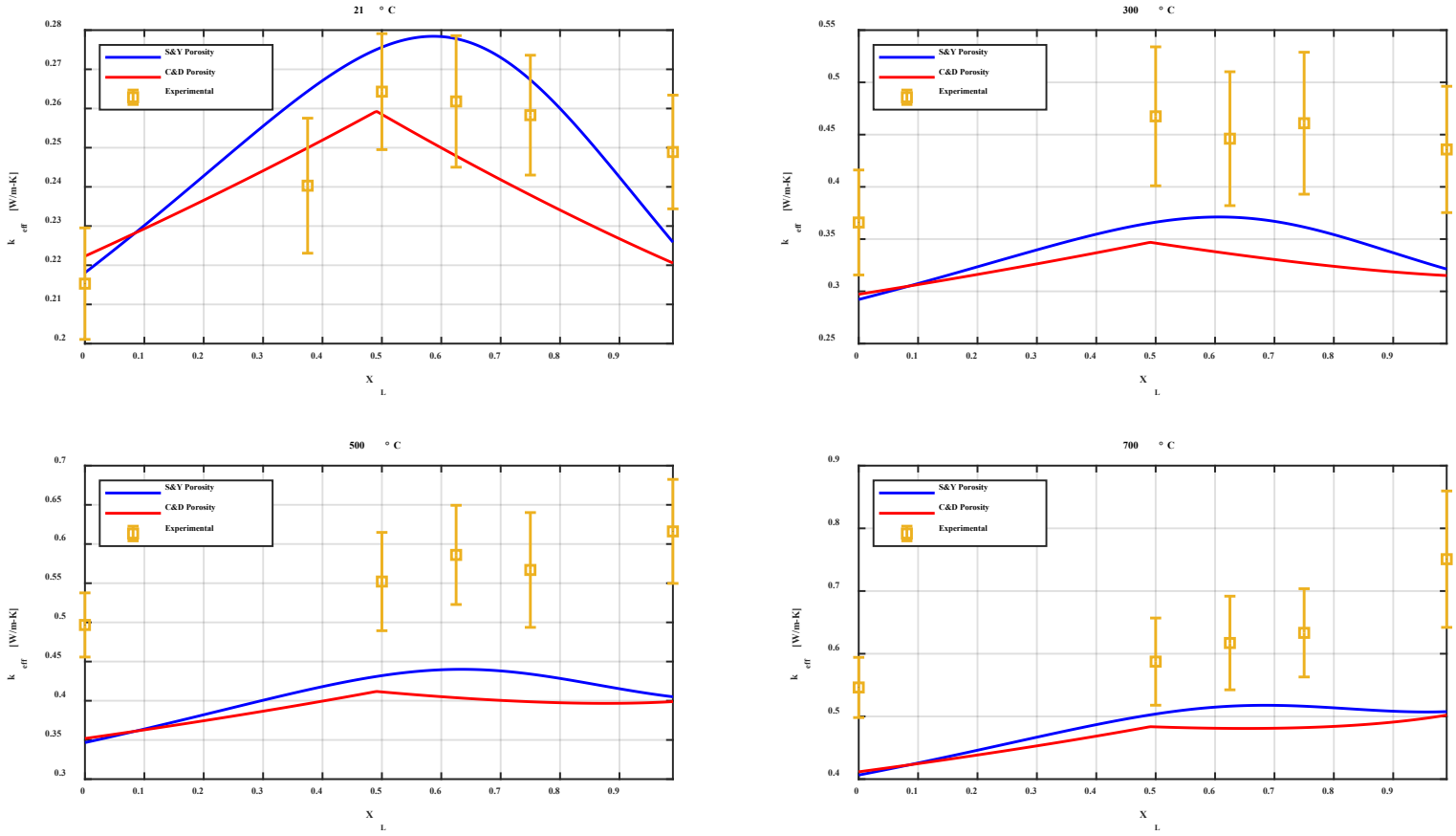

Figure 2.15 Large particle volume fraction vs. effective thermal conductivity for a variety of temperatures. The blue lines are the ZBS models with the Standish and Yu porosity models and the red lines are the ZBS thermal conductivity models with the Chang and Deng porosity models.

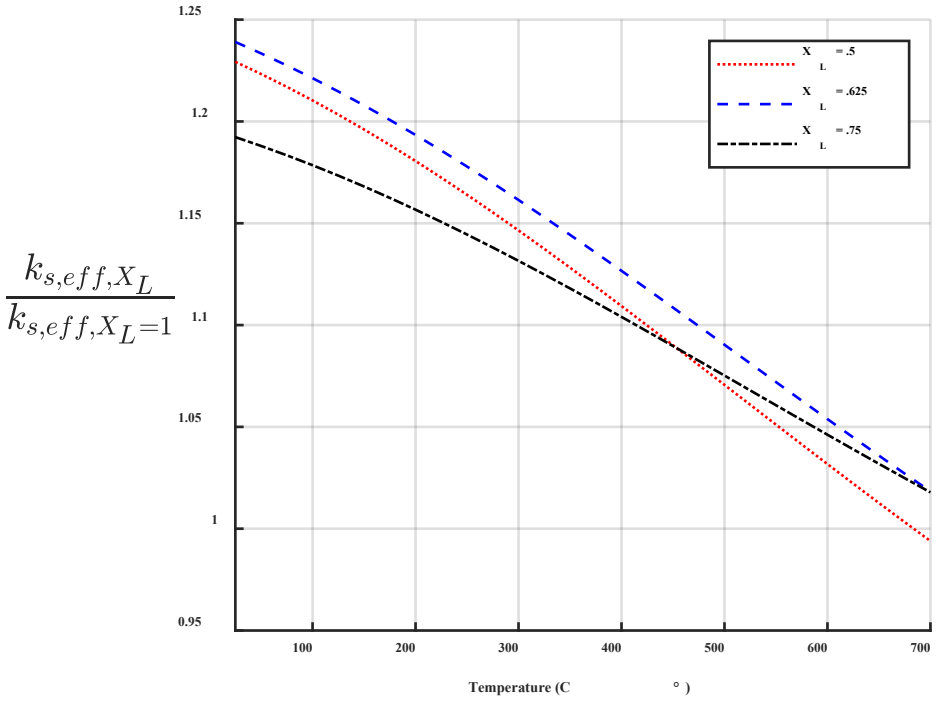

Figure 2.16 Ratio of the ZBS calculated bulk effective thermal conductivity at X_L and X_L = 1 (HSP particles) plotted against temperature for the HSP 16/30-40/70 mixture.

Figure 2.16 illustrates how the ZBS modeled large particle volume fractions vary when compared to a pure HSP 16/30 particle distribution. The ZBS model shows that binary particle distributions are superior up to around 700 °C. Extrapolating beyond 700 °C would indicate that pure HSP 16/30 particle distributions have higher thermal conductivities than any HSP 16/30-40/70 binary mixture.

A parametric study of the ZBS model for all size ratios and large particle volume fractions for an HSP particle mixture having the large particle of HSP 16/30 can be found in Figure 2.17. The contour plots in Figure 2.17 analyze the thermal conductivity of an HSP 16/30 particle and any other particle smaller than itself in diameter. The size of the small particle determines the size ratio. The size ratio coupled with the large particle volume fraction determines the thermal conductivity for that particle mixture. Vertical

blue lines can be seen in Figure 2.17 which represent the exact size ratio of the HSP 16/30-40/70 particle mixture. These represent the data found in Figure 2.15. The contour maps only utilize the Standish and Yu porosity model as the Chang and Deng model requires experimentally determined parameters for every size ratio.

The importance of Figure 2.17 and contour mapping thermal conductivities lies in its ability to quickly illustrate the heat transfer potential for a large combination of particles. In this manner, optimal particle mixtures for specific scenarios can be easily determined. With respect to Figure 2.17, we see that the ZBS model projects that a low size ratio coupled with a large particle volume fraction of about .7 yields the highest thermal conductivity. According to the ZBS model, the best thermal conductivity obtainable would require using a small particle around $1/10^{th}$ the size of an HSP 16/30 particle with about 70% of the mixture being the HSP 16/30 particle. However, in reality, particle self-segregation or particle stratification begins to hinder effectiveness of heat transfer in binary particle mixtures for size ratios below .5. More research in this area is needed to understand what the lower limitations of the size ratio are but it is understood that lower size ratios cause smaller particles to sift to the bottom of the particle mixture and essentially create a monodispersed distribution [50]. Other restrictions would be using too small diameters or particles too large as this also might cause adverse effects on the heat transfer of the media.

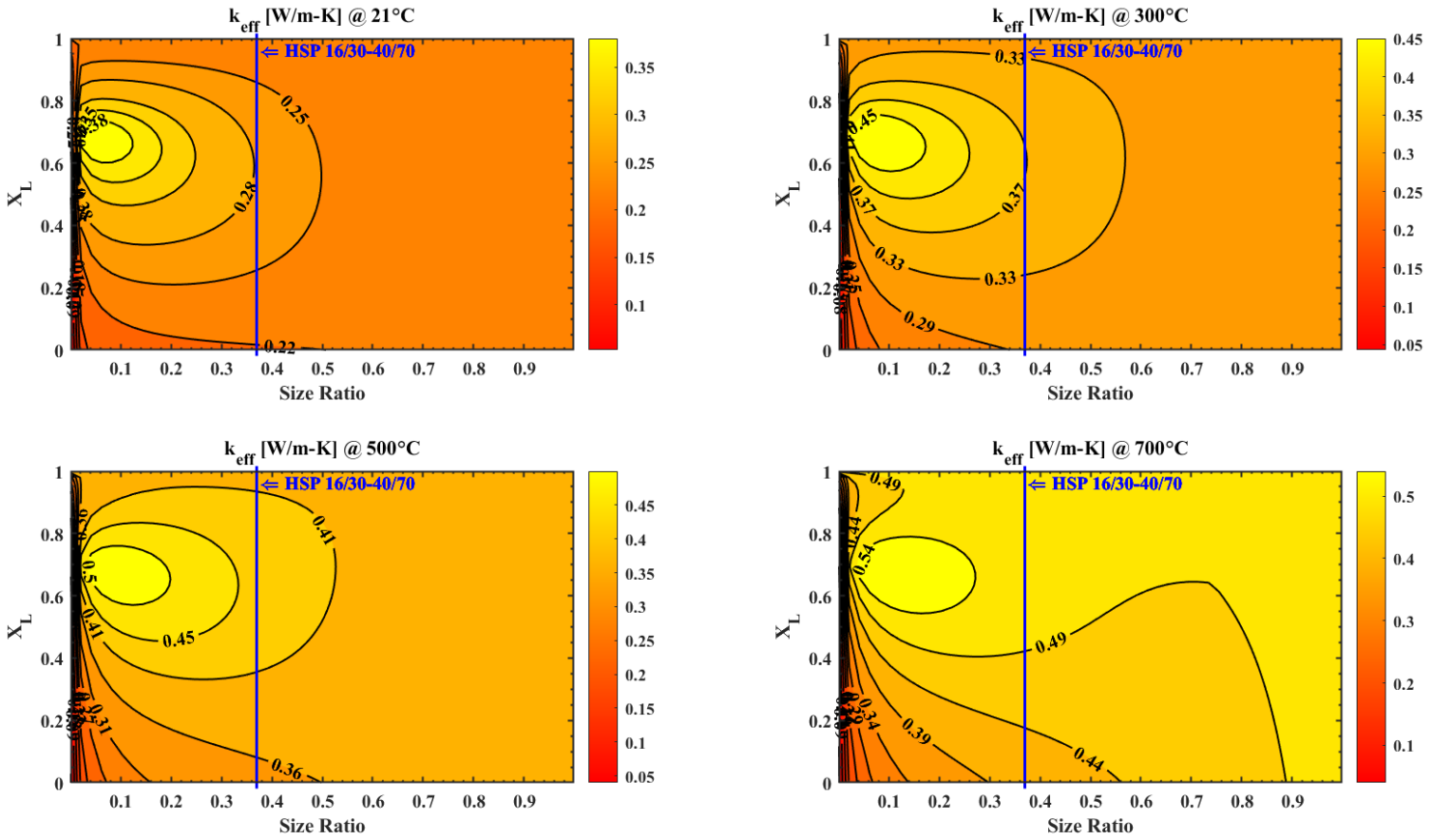

Figure 2.17 Size ratio and large particle volume fraction vs. effective thermal conductivity contour plots for a variety of temperatures using the ZBS thermal conductivity model. The vertical blue lines represent the HSP 16/30-40/70 particle distribution size ratio where data was collected. Contour maps only utilize the Standish and Yu porosity model as the Chang and Deng model requires experimentally determined parameters for every size ratio.

2.4.5 HSP Yagi and Kunii Results

Figure 2.18 illustrates the modeled thermal conductivities for the Yagi and Kunii model with both porosity models. Figure 2.18 reveals that the Yagi and Kunii model does not match the experimental data at ambient temperatures. The ZBS parabolic shape evident in Figure 2.15 at ambient temperature better resembles the experimental data when compared to the Yagi and Kunii model at the same temperature. The Yagi and Kunii model does resemble the shape of the experimental data at 700 °C. However, modeled values are significantly higher than experimental results.

Figure 2.19 illustrates how the Yagi and Kunii modeled large particle volume fractions vary when compared to a pure HSP 16/30 particle distribution. The Yagi and Kunii model shows that binary particle distributions are superior up to ~275 °C. Beyond this, pure HSP 16/30 particle distributions have higher thermal conductivities than any HSP 16/30-40/70 binary mixture. Contour plots depicting Yagi and Kunii thermal conductivity model for various size ratios and large particle volume fractions can be found in Figure 2.20. The Yagi and Kunii contour plots differ significantly from those of the ZBS. At ambient temperatures, the ZBS model in Figure 2.17 illustrates that small size ratios will deliver the greatest thermal conductivity. From 300-700 °C, the Yagi and Kunii model projects that the optimal thermal conductivity that can be obtained is by utilizing a size ratio near 1. In other words, the Yagi and Kunii model shows that a monodisperse particle distribution composed of larger particles yields the most thermally conductive particle mixture. This narrative agrees with the experimental data at high temperatures only.

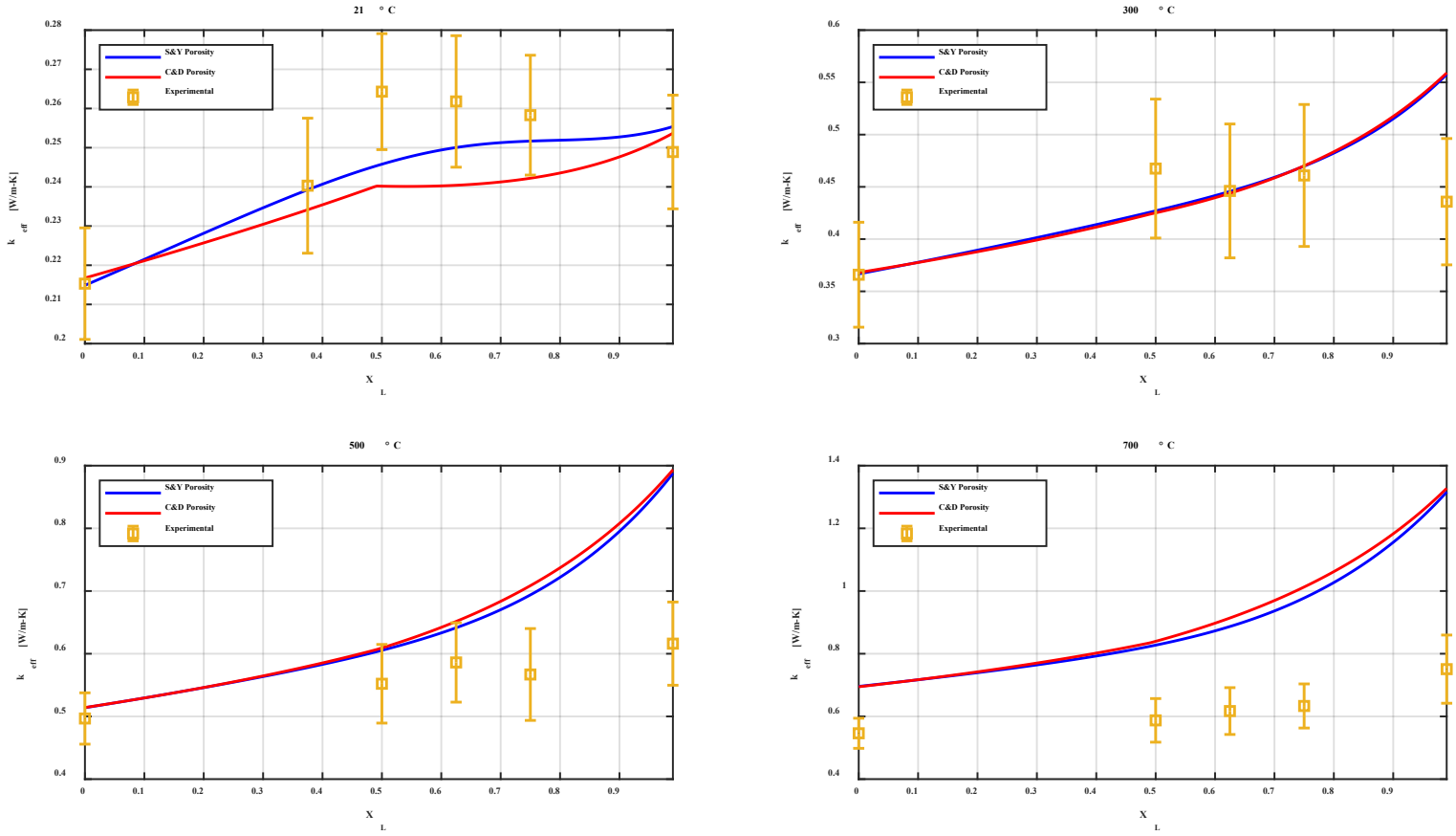

Figure 2.18 Large particle volume fraction vs. effective thermal conductivity for a variety of temperatures. The blue lines are the Yagi and Kunii models with the Standish and Yu porosity models and the red lines are the Yagi and Kunii thermal conductivity models with the Chang and Deng porosity models.

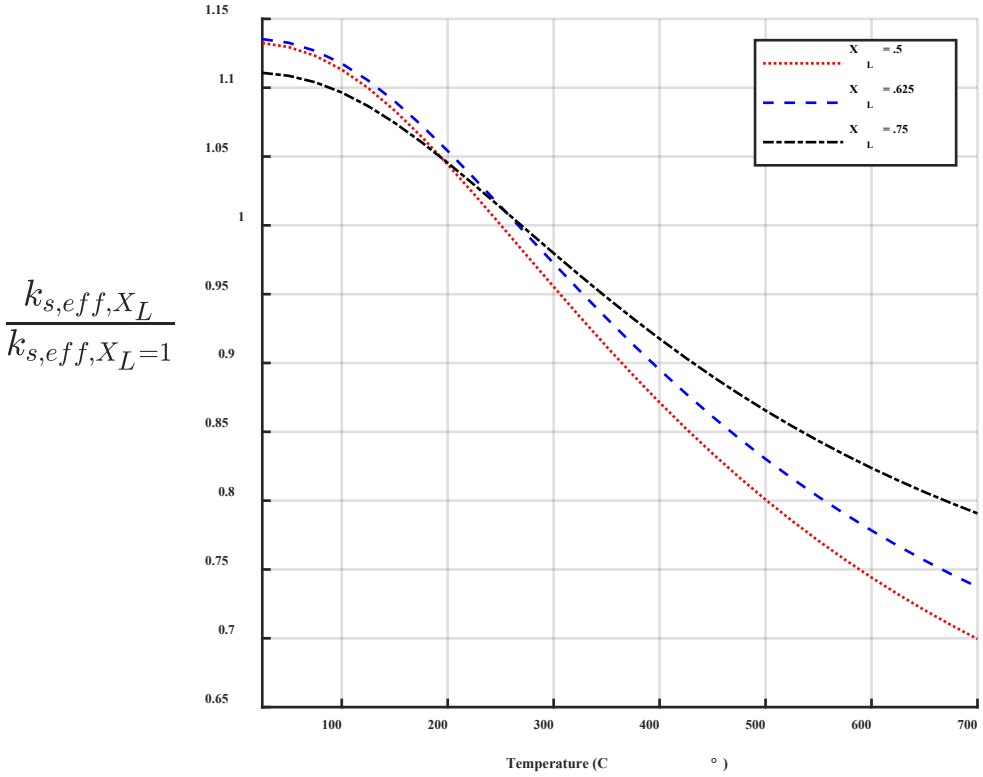

Figure 2.19 Ratio of the Yagi and Kunii calculated bulk effective thermal conductivity at X_L and X_L = 1 (HSP particles) plotted against temperature for the HSP 16/30-40/70 mixture.

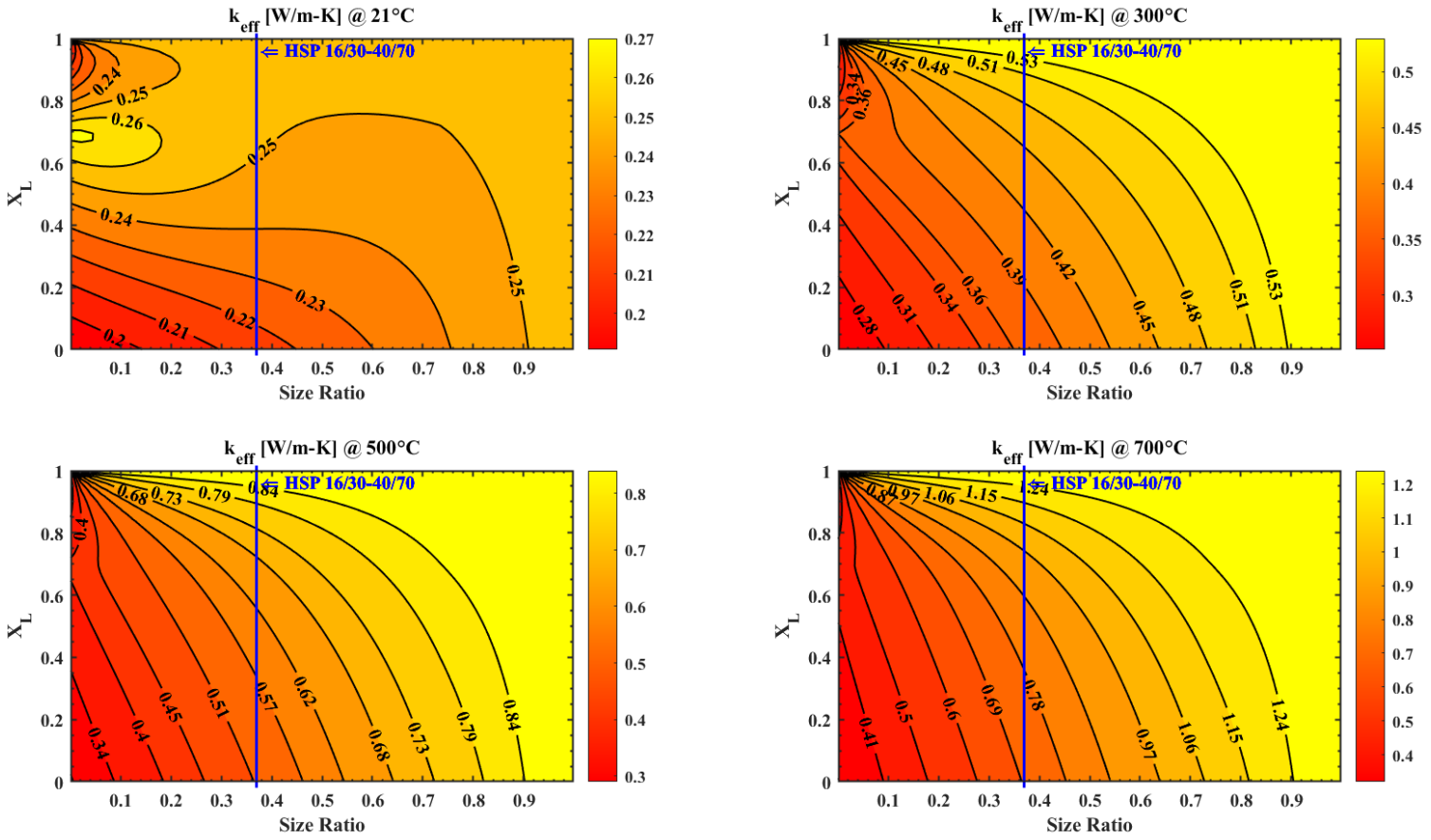

Figure 2.20 Size ratio and large particle volume fraction vs. effective thermal conductivity contour plots for a variety of temperatures using the Yagi and Kunii thermal conductivity model. The vertical blue lines represent the HSP 16/30-40/70 particle distribution size ratio where data was collected. Contour maps only utilize the Standish and Yu porosity model as the Chang and Deng model requires experimentally determined parameters for every size ratio.

2.5 Variation of Results with Measurement Technique

Variations in near-wall porosity are difficult to account for as there are limited studies on how thermal conductivity changes with these variations. An inspection of Figure 2.21 illustrates the variation of measured thermal conductivity in a fresh pour where particles are replaced. This variation is visibly greater than that of a stale pour where the particles were not replaced after every test. Fresh and stale particle test statistics are outlined in Table 2.4. Recall Table 2.1 where the recorded porosities calculated with a graduated cylinder show variation of only around .35-1.23%. Variations in thermal conductivity of fresh pours are around 2.21-4.92% and stale pours around .51-2.44% as displayed in Table 2.4. The porosity of the particle mixture for both fresh and stale pours most likely only varies from around .35-1.23% as demonstrated. Variation in thermal conductivity for stale pours of .51-2.44% is not likely due to changes in bulk or near-wall porosity as the particles are not replaced after each test. Therefore, this level of variation is likely primarily due to the instrument accuracy of the Hot Disk TPS 2500-S.

The larger variation of the thermal conductivities of the fresh pours is most likely due to variations in near wall porosity as the general bulk porosity of the particle mixtures was only shown to vary by around .35-1.23%. Variations in near wall porosity are difficult to account; especially when dealing with bimodal particle distributions. This is because smaller particles occasionally tend to sift to the bottom of the mixture at the sensor-particle interface or the “near-wall”. This self-segregation likely leads to higher levels of variation in recorded thermal conductivities as evidenced by the 2.21-4.92% thermal conductivity variation for fresh pours. More research is needed to understand this behavior and validate this theory.

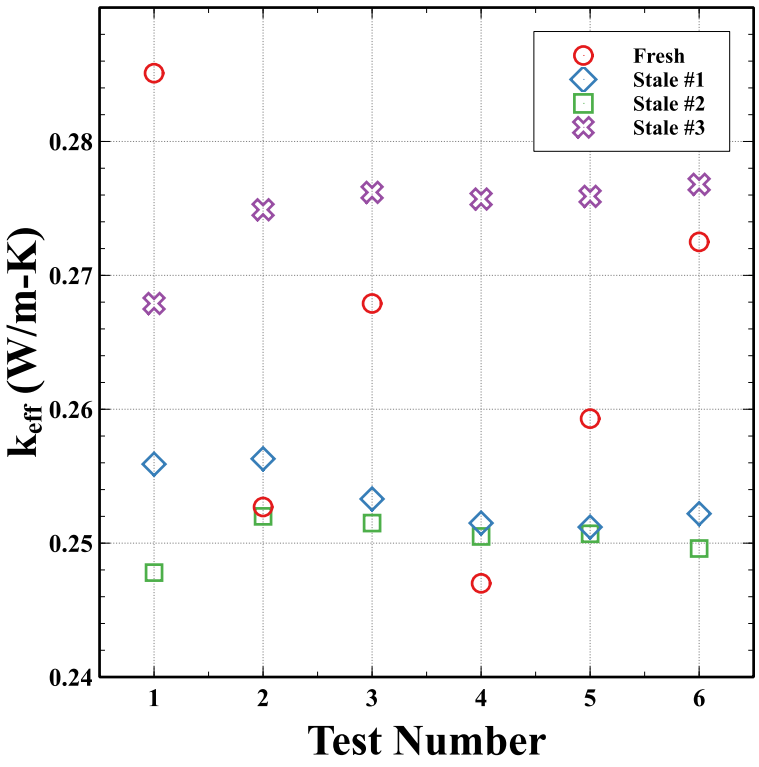

Figure 2.21 Variation in thermal conductivity between tests for HSP 16/30-40/70 at X_L = .625. Note the small variation for stale tests where the particles were not replaced between each test and the large variation between fresh tests where the particles were replaced between each test.

Table 2.4 Particles tested in this study. Particle properties can be seen in the CARBOBEAD data sheet [28] with the exception of the measured particle diameter.

Material	% Variation in Thermal Conductivity	
	Particles replaced	Particles not replaced
HSP 40/70	3.53%	2.44%
HSP 16/30 – HSP 40/70, X_L = 0.50	4.92%	1.34%
HSP 16/30 – HSP 40/70, X_L = 0.625	4.81%	0.89%
HSP 16/30 – HSP 40/70, X_L = 0.75	3.29%	0.51%
HSP 16/30	2.21%	1.87%

CHAPTER THREE: HEAT EXCHANGER MODELING

3.1 An Introduction to Particle-to-sCO_2 Heat Exchangers

Fundamental in any solar thermal facility is the process and efficiency of transferring heat from one source to another. This is accomplished with a heat exchanger and will be explained in both the literal and mathematical sense here.

3.1.1 The Shell-and-Plate Particle-to-sCO_2 Heat Exchanger

The high-temperature durability of solid particles has garnered substantial interest for integration with high-efficiency power cycles over the past decade [51]. One promising technology that potentially could be driven by the heat transfer capabilities of solid particles is the supercritical CO_2 (sCO_2) power cycle [52]. A primary goal for particle-to-sCO_2 power cycles is to heat sCO_2 upwards of 720 °C [53], well below the temperatures solid particles are stable at.

Typically, particle-to-sCO_2 heat exchangers are categorized into either one of two configurations: fluidized and moving packed-bed. Generally, the fluidized bed configuration has been observed to have a higher overall heat transfer coefficient when compared to its moving packed-bed counterpart. However, this advantage in U requires the use of components such as fluidization gas compressors and recuperative heat exchangers which inhibit the configuration from a cost-effectiveness standpoint [12]. Moreover, moving packed-bed configurations have been examined through multiphase CFD simulations and have been determined to potentially be the more cost-effective and simpler option [54]. This viewpoint is confirmed in the study performed by Ho et. al. where both fluidized bed and shell-and-plate particle-to-sCO_2 heat exchangers were examined. The final weighted score for the two classes of heat exchanger based on cost,

heat-transfer coefficient, structural reliability, manufacturability, parasitics and heat losses, scalability, compatibility, erosion and corrosion, transient operation, and inspection ease revealed that shell-and-plate heat exchanger configurations are the most viable and manufacturable option for particle-to-sCO_2 thermal transfer [10].

Sandia National Laboratory (SNL) has extensively researched shell-and-plate particle-to-sCO_2 moving packed-bed heat exchangers, developed predictive models to evaluate how particle size and heat exchanger component geometries effect overall performance [37] and has examined high-temperature particle flow experimentally [12]. SNL examined a 100 kW_t particle-to-sCO_2 shell-and-plate moving packed-bed heat exchanger at intermediate temperatures (<500 °C) and measured a low overall heat transfer coefficient of 50-80 W/m^2-K when compared to their anticipated heat transfer coefficient of 150 W/m^2-K [55]. Findings revealed that the low overall heat transfer coefficient was the result of particle flow non-uniformity, sCO_2 flow non-uniformity, and high sCO_2 pressure drop. Furthermore, SNL identified that reducing heat exchanger plate spacing to enhance the particle side heat transfer coefficient and moving to a single bank pure counter-flow heat exchanger are imperative in optimizing the overall heat transfer coefficient.

Recently, SNL has designed and tested a prototype next-generation particle-to-sCO_2 shell-and-plate moving packed-bed heat exchanger resulting in much more impressive overall heat transfer coefficients of ~300 W/m^2-K at 17 MPa and particle inlet temperatures of 500 °C [56]. SNL projects that high-temperature approaches with this prototype could result in peak overall heat transfer coefficients of ~400 W/m^2-K. This 400 W/m^2-K threshold will be more easily achieved as initial next-generation particle

receiver designs have demonstrated the ability to achieve and maintain particle outlet temperatures approaching 800 °C [57]. Finally, the interest of SNL in particle-to-sCO_2 shell-and-plate moving packed-bed heat exchangers is due to the Gen 3 Particle Pilot Plant (G3P3) project sponsored by the U.S. Department of Energy's Solar Energy Technologies Office. The goal of G3P3-USA is to design, construct, and operate a pilot-scale system that heats particles from ~600 °C to ~775 °C in a >1 MW_t FPR with 6 MWh of thermal storage where sCO_2 is heated from ~565 °C to ~715 °C at ~20-25 MPa [58]. While much of the groundwork for this project has already been laid, the heat exchanger modeling that will be outlined in this chapter will aid in particle selection, which is critically dependent on the packed-bed properties.

3.1.2 Overall Heat Transfer Coefficient Calculation

Fundamentally speaking, the purpose of a heat exchanger is to facilitate the transfer of thermal energy from one medium to another. For this reason, the properties of the heat transfer media employed is of critical importance and works to optimize the overall heat transfer coefficient, *U*. Albrecht and Ho's definition of the overall heat transfer coefficient for a moving packed-bed shell-and-plate particle-to-sCO_2 heat exchanger can be expressed as follows: [12]:

$$U = \left(\frac{1}{\bar{h}_{sCO_2}} + \frac{t_w}{k_m} + R_c^{''} + \frac{1}{\bar{h}_{sw}}\right)^{-1} \tag{51}$$

where $\bar{h}_{sCO_2}$ is the average sCO_2 convection coefficient, t_w is the heat exchanger wall thickness, k_m is the heat exchanger media thermal conductivity, $R_c^{''}$ is the particle-wall contact resistance, and $\bar{h}_{sw}$ is the average particle-wall convection coefficient. It then follows that the energy transfer is

$$Q = UA \cdot \Delta T_{lm} \tag{52}$$

where U is the overall heat transfer coefficient, A is the heat transfer surface area and ΔT_{lm} is the log mean temperature difference (LMTD) between both the inlet and outlet particle and sCO_2 streams. ΔT_{lm} can be calculated by the following:

$$\Delta T_{lm} = \frac{(T_{s,out} - T_{sCO_2,in}) - (T_{s,in} - T_{sCO_2,out})}{\ln\left(\frac{T_{s,out} - T_{sCO_2,in}}{T_{s,in} - T_{sCO_2,out}}\right)} \tag{53}$$

Finally, Albrecht and Ho explain that the heat exchanger effectiveness can be expressed as [12]

$$\varepsilon_{HX} = \frac{Q}{\dot{m}_s c_{p,s}(T_{s,\,in} - T_{sCO_2,\,in})} \tag{54}$$

where $\dot{m}_s$ is the mass flow rate of the particles, $c_{p,s}$ is the specific heat of the particles and $T_{s,\,in}$ and $T_{sCO_2,\,in}$ are the inlet temperatures of both the particles and the sCO_2 streams.

Figure 3.1 illustrates how heat exchanger effectiveness can be significantly impacted by the thermal conductivity of the heat transfer media employed in an FPR CSP facility.

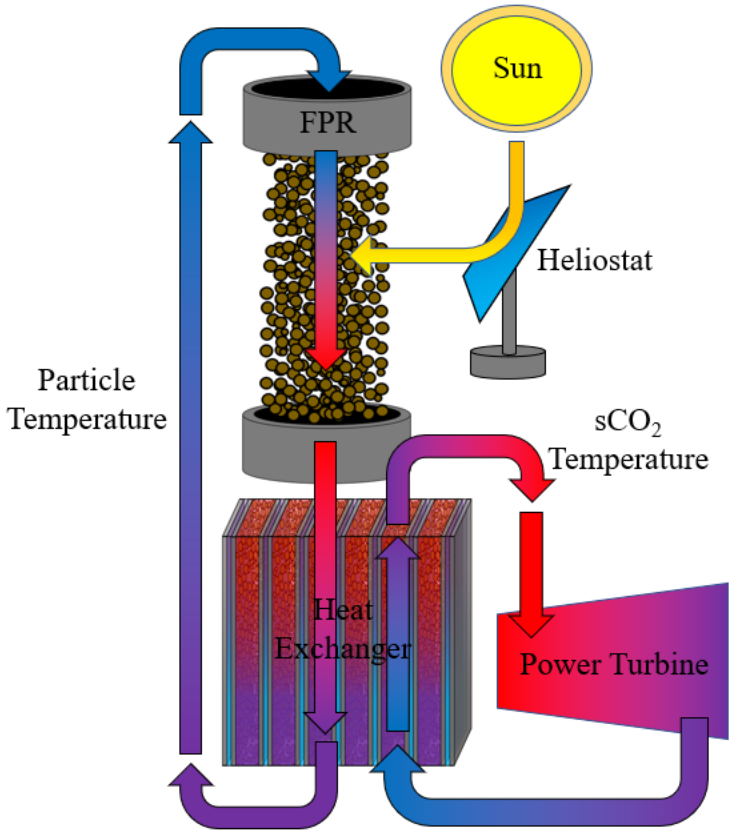

Figure 3.1 Temperature path profiling of particles and sCO_2 throughout heat exchange process in an FPR facility.

3.2 Numerical Model Description

3.2.1 Model Physical Dimensions and Input Parameters

Albrecht and Ho of SNL developed a counterflow shell-and-plate moving packed-bed heat exchanger model capable of analyzing the heat transfer effect of particle size, operating temperature and particle velocity [37]. This model, coupled with the Sauter mean diameter [31], allows further investigation into not only the heat transfer effect of particle size but of binary particle mixtures. Figure 3.2 illustrates the physical model that will be employed where a single vertical particle channel will be the focus of the overall simulation. From Figure 3.2, t_{sCO_2} is the width of the sCO_2 channel, t_w is the width of the channel wall divider, t_s is the width of the particle channel. $T_{s,in}$ and $T_{s,out}$ are the

temperatures of the incoming and outgoing particles, respectively. Similarly, $T_{sCO_2,\,in}$ and $T_{sCO_2,\,out}$ are the temperatures of the incoming and outgoing sCO_2. L is the length of the particle channel and W is the width.

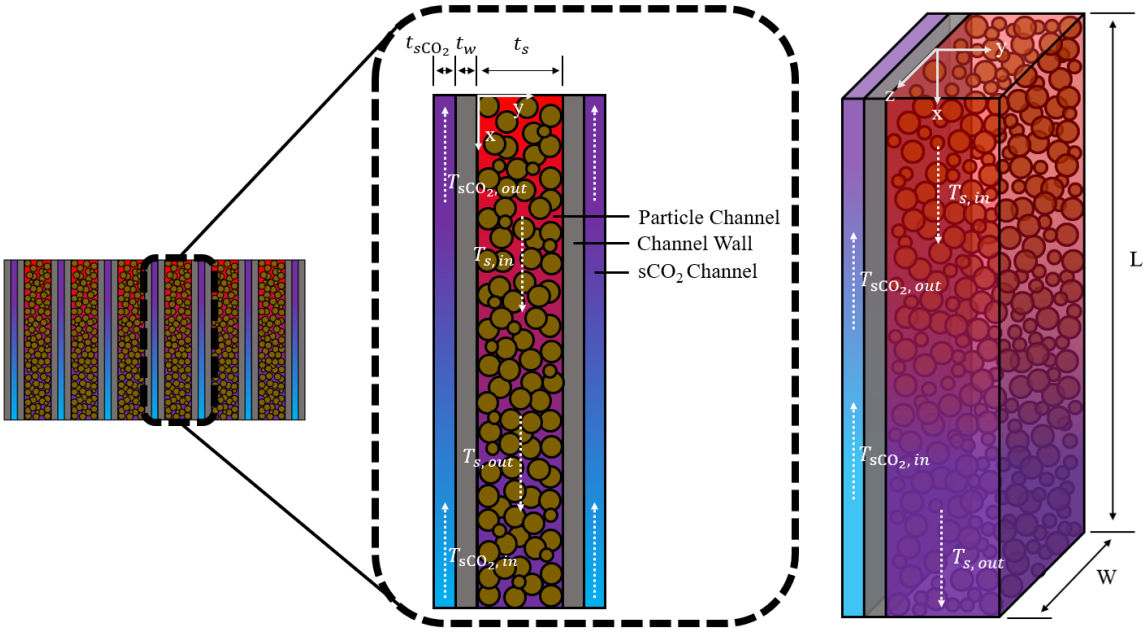

Figure 3.2 Counterflow shell-and-plate moving packed-bed heat exchanger diagram for use in numerical modeling. The left diagram illustrates a single bank configuration, while the center and right illustrate 2D and 3D angles of a single particle channel within a bank.

3.2.2 Governing Equations and Numerical Model Assumptions

Critical to the heat transfer of the particles to the sCO_2 are the mass flow rates of each. For modeling purposes, it is assumed that the mass flow rates of each are constant. These flow rates are determined by using the conservation of energy principle. For the particles:

$$\dot{Q}_{HX} = \dot{m}_s c_{p,s}(T_{s,in} - T_{s,out}) \tag{55}$$

And for the sCO_2:

$$\dot{Q}_{HX} = \dot{m}_{sCO_2}\left[h_{sCO_2}\left(T_{sCO_2,in}, P_{sCO_2}\right) - h_{sCO_2}\left(T_{sCO_2,out}, P_{sCO_2}\right)\right] \tag{56}$$

where h_{sCO_2} is the enthalpy of the sCO_2 and P_{sCO_2} is the pressure. It is assumed that there is not a pressure drop in the sCO_2 across a singular bank. Full-scale CFD analysis on compact microchannel sCO_2 heat exchangers, commonly referred to as Printed Circuit Heat Exchangers (PCHE), has demonstrated that the pressure drops within sCO_2 channels is not negligible [61]. However, incorporation of these complex sCO_2 pressure modeling procedures will not be applied here. An assumption can also be made concerning the equilibrium state of the particles and the air [62]. Because of this, there is only particle-to-particle conduction in the y-direction. Furthermore, a similar assumption can be made for the sCO_2 temperature variation in the x-direction as the sCO_2 convection coefficient has been well established [11] and no heat source or sink is present in the numerical model.

Albrecht and Ho [37] define the 1-D steady-state conservation of energy equation for the sCO_2 and the 2-D steady state conservation of energy for the particles as

$$\rho_{sCO_2} v_{sCO_2} c_{p,\,sCO_2} \frac{dT_{sCO_2}}{dx} = \frac{2q''}{t_{sCO_2}} \tag{57}$$

$$\rho_s v_s c_{p,s} \frac{dT_s}{dx} = \frac{\partial}{\partial y}\left(k_{s,eff} \frac{\partial T_s}{\partial y}\right) \tag{58}$$

Discretizing equation (58) in the y-direction creates a set of ordinary differential equations which can be numerically solved with MATLAB's ode15s function. Interior nodes analyzed in this manner have a 2nd order central differencing [44] enforced upon them taking the form of

$$\left.\frac{\partial^2 T_s}{\partial y^2}\right|_{x,y} = k_{s,eff} \frac{T_s(y-1,x) - 2T_s(y,x) + T_s(y+1,x)}{\rho_s v_s c_{p,s} (\Delta y)^2} \tag{59}$$

Moreover, the boundary condition occurring at the particle wall divider and the first layer of particles also utilizes a 2nd order central differencing technique with equations in the x-direction taking the form of

$$\left.\frac{dT_s}{dy}\right|_{0,x} = \frac{2q"}{v_s\rho_s c_{p,s}\Delta y} - \frac{2k_{s,eff}\left(T_s(0,x)-T_s(1,x)\right)}{v_s\rho_s c_{p,s}(\Delta y)^2} \tag{60}$$

Halfway through the particle channel in the y-direction, symmetric behavior can be identified. Due to this phenomenon, the following boundary condition can be applied:

$$\left.\frac{dT_s}{dy}\right|_{\frac{t_s}{2},\, x} = 0 \tag{61}$$

By coupling the sCO_2 and particles regions of the numerical model found in equations (57) and (58), the local heat flux can be matched and expressed as

$$q"(x) = k_{s,eff}\left.\frac{dT_s}{dy}\right|_{0,\, x} = \frac{1}{R"(x)}\left(T_s(0,x) - T_{sCO_2}(x)\right) \tag{62}$$

where *R"* is the specific thermal resistance. This can be written as follows:

$$R" = \left(\frac{1}{\bar{h}_{sw}} + \frac{t_w}{k_w} + R_c^{"} + \frac{1}{\bar{h}_{sCO_2}}\right) \tag{63}$$

Here, the average particle wall convection coefficient is $\bar{h}_{sw}$, the particle near-wall contact resistance is represented as $R_c^{"}$, the sCO_2 convection coefficient is denoted by $\bar{h}_{sCO_2}$, and the particle wall conduction resistance can be expressed as $\frac{t_w}{k_w}$. $R_c^{"}$ can then be expressed as

$$R_c'' = \frac{d_p}{2k_{s,eff}^{nw}} \tag{64}$$

where $k_{s,eff}^{nw}$ is the thermal conductivity of the near wall region. When approaching the near wall of the particle channel, the bulk thermal conductivity is no longer a good representation of the particle thermal conductivity because the porosity decreases as

discovered by Denloye and Botterill [63]. From their research, they determined that the near wall porosity for a monodispersed particle distribution can be calculated by

$$\varepsilon_{nw} = \frac{(1-\varepsilon)(0.7293+0.5139Y)}{1+Y} \tag{65}$$

where ε is the bulk porosity and Y is defined as

$$Y = \frac{d_p}{2a} \tag{66}$$

Here, a is the radius of the heat transfer surface. For flat plates, similar to the channel walls that particles traverse, a is infinity and therefore, Y is equal to zero. CFD simulations using radial porosity profiling have shown good agreement with this ZBS approach [64] and for this reason, an alternative near-wall porosity approach for thermal conductivity at the near-wall is justifiable. Therefore, the ZBS thermal conductivity at the near wall is calculated not with the bulk porosity ε, but with the near wall porosity ε_{nw}.

In simulation, iterations are carried out through particle and sCO_2 mass flow updates until the following boundary conditions are satisfied:

$$T_{sCO_2}(\mathrm{x} = 0) = T_{sCO_2,in} \tag{67}$$

$$T_{sCO_2}(x = H) = T_{sCO_2,out} \tag{68}$$

$$T_s(0, y) = T_{s,in} \tag{69}$$

$$\frac{1}{t_s}\int_0^{t_s} T_s(H, y)dy = T_{s,out} \tag{70}$$

where H is total length of the particle channel. Once the boundary conditions listed in equations (67-70) are satisfied and the simulation has been completed, the heat transfer rate, Q, is summed and the overall heat transfer coefficient for the heat exchanger is calculated with equations (51) and (52). Figure 3.3 illustrates a discretized particle

channel where the aforementioned boundary conditions can be interpreted. The x and y-directions can be discretized into any number of nodes.

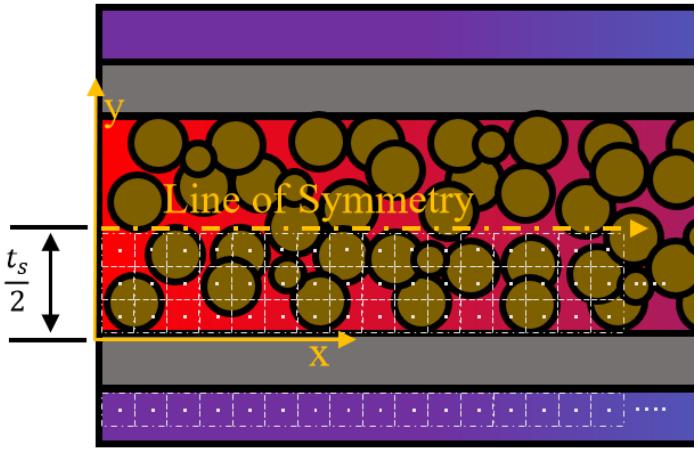

Figure 3.3 Discretized particle channel. By utilizing the symmetry of the particle channel, significant computational resources can be saved.

3.2.3 Particle and sCO_2 Convection

Critical to the overall heat transfer of the heat exchanger is the convection of not only the particles but of the sCO_2. The numerical model follows the Gnielinski correlation sCO_2 convection coefficient [65]:

$$h_{sCO_2} = \frac{Nu_{D_h} k_{sCO_2}}{D_{h,sCO_2}} = \frac{k_{sCO_2} 0.0214\left(Re^{0.8}-100\right)Pr^{0.4}\left[1+\left(\frac{D_{h,sCO_2}}{L}\right)^{\frac{2}{3}}\right]\left(\frac{T_{m,sCO_2}}{T_w}\right)^{0.48}}{D_{h,CO_2}} \tag{71}$$

where T_{m,sCO_2} is the mean temperature of the sCO_2 and T_w is the wall temperature. Additionally, D_{h,sCO_2} is the hydraulic diameter, Re is the Reynolds number and Pr is the Prandtl number all of which can be expressed as follows:

$$D_{h,CO_2} = \frac{4t_{sCO_2}W}{2(t_{sCO_2}+W)} \approx 2t_{sCO_2} \; for \; W \gg t_{sCO_2} \tag{72}$$

$$Re = \frac{v_{sCO_2} D_{h,sCO_2} \rho_{sCO_2}}{\mu_{sCO_2}} \tag{73}$$

$$Pr = \frac{\mu_{sCO_2} c_{p,sCO_2}}{k_{sCO_2}} \tag{74}$$

The numerical model takes an isobaric approach to the sCO_2 and all properties are evaluated at the average temperature as per the Span and Wagner correlations [66] and the average wall temperature. The nature of the boundary conditions for the simulation causes the values of k_{CO_2}, T_m, T_w, and Pr to remain nearly constant for each simulation.

The particle-wall convection can be calculated by using the Nusselt number relationship for the analytical solution of plug flow in a moving packed-bed parallel plate heat exchanger [67]:

$$\overline{Nu}_{Dh,H} = \frac{\bar{h}_{sw} D_h}{k_{s,eff}} = \left[\left(2 \frac{0.886}{\sqrt{Gz^{-1}}} \right)^{\frac{12}{5}} + 12^{\frac{12}{5}} \right]^{\frac{5}{12}} \tag{75}$$

Equation (75) is utilized as Watkins and Gould found good agreement between the correlation of circular and rectangular channels [68]. Gz^{-1} is the inverse Graetz number, a nondimensional number that is traditionally used to characterize the transient heat conduction in pipes with laminar flow [69]. This can be written as

$$\mathrm{Gz}^{-1} = \frac{L}{Pe_{D_h} D_h} \tag{76}$$

Here, Pe is the Peclet number and can be expressed as follows:

$$Pe_{D_h} = \frac{v_s D_h}{\alpha_s} \tag{77}$$

where α_s is the thermal diffusivity of the particles. Finally, the hydraulic diameter of the particle flow is D_h, expressed as

$$D_h = \frac{4 t_s W}{2(t_s + W)} \approx 2 t_s \; for \; W \gg t_S \tag{78}$$

3.3 Monodisperse Particle Distribution Modeling

Before the performance of binary particle distributions in a heat exchanger model can be explored, a baseline must be established. This can be done by analyzing how a monodisperse particle distribution perform in the same heat exchanger model.

3.3.1 G3P3 20 kW_t Prototype Numerical Model Geometry and Boundary Conditions

Sandia National Laboratory currently is researching and developing the world's first 1 MW_t heat exchanger under the Gen3 Particle Pilot Plant (G3P3) program [56]. As part of this effort, a 20 kW_t shell-and-plate moving packed-bed prototype heat exchanger is currently being constructed. This particular heat exchanger will utilize the following boundary conditions [37], [56]:

$$T_s(0, y) = T_{s,in} = 500\ °C \tag{79}$$

$$\frac{1}{t_s}\int_0^{t_s} T_s(H, y)dy = T_{s,out} = 340\ °C \tag{80}$$

$$T_{sCO_2}(\mathrm{x} = 0) = T_{sCO_2,in} = 290\ °C \tag{81}$$

$$T_{sCO_2}(x = H) = T_{sCO_2,out} = 450\ °C \tag{82}$$

Key input parameters for modeling the G3P3 20 kW_t prototype in this work can be found in Table 3.1.

Table 3.1 HSP 40/70 counterflow shell-and-plate moving packed-bed heat exchanger modeling parameters for .

Property	Symbol	Value	Units	Ref.
sCO_2 Pressure	P_{CO_2}	17	MPa	[56]
Particle Specific Heat	C_p	1280	J kg^{-1} K^{-1}	[59]
Particle Thermal Conductivity	k_s	2.0	W m^{-1} K^{-1}	[11]
Bulk Particle Density	ρ_s	3610	kg m^{-3}	[28]
HX Length	L	348.5	mm	[56]
HX Width	W	139.4	mm	[56]
HX wall thickness	t_w	1	mm	[37]
HX wall thermal conductivity	k_w	23	W m^{-1} K^{-1}	[59]
sCO2 channel thickness	t_{CO_2}	1.2	mm	[11]
Particle channel thickness	t_s	3.0	mm	[56]
Particle flow rate	$\dot{m}_s$	112	g/s	[56]

A CAD drawing of the G3P3 20 kW_t prototype from SNL's performance review of the heat exchanger can be seen in Figure 3.4. The 20 kW_t prototype consists of 7 parallel plates with 3 mm particle channels that generate 12 surfaces that are available for particle heat transfer, each with an effective surface area of .0486 m^2. Using the length-to-width aspect ratio of 2.5 for the G3P3 20 kW_t prototype heat exchanger [56] that can be seen in Figure 3.4 and the effective heat transfer surface area of .0486 m^2, a length of .3485 m and a width of .1394 m is appropriate for the heat exchanger geometry in the numerical model.

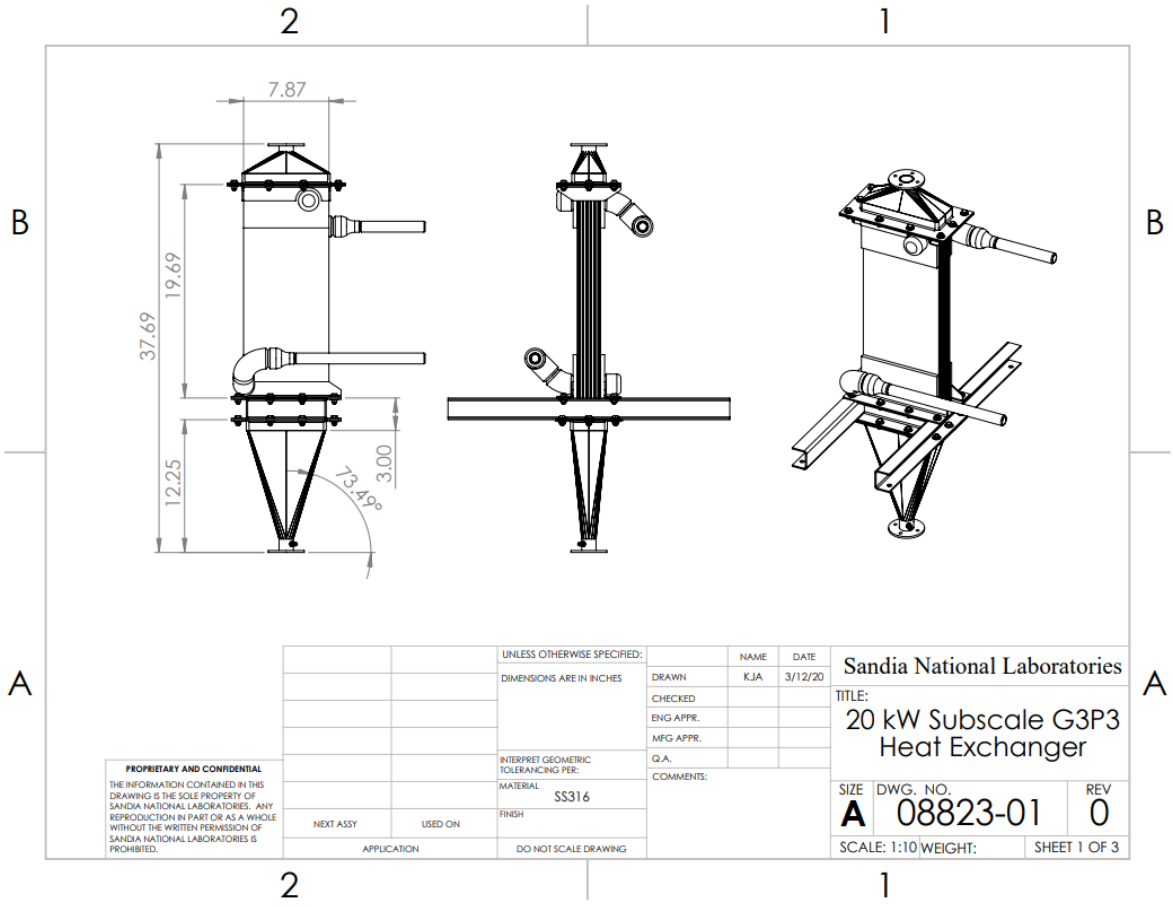

Figure 3.4 CAD drawing of the G3P3 20 kW_t prototype from SNL's performance review of the heat exchanger. Note the length-to-width aspect ratio of the heat exchanger in inches (19.69/7.87) which is used with the effective heat transfer surface area (.0486 m^2) to determine appropriate numerical modeling geometry. Adopted from [56]**.**

3.3.2 Benchmarking with SNL's G3P3 20 kW_t Prototype Model Simulation

From simulation, the temperature gradient of the discretized domain and the full particle channel domain can be seen in Figure 3.5. Utilizing the symmetry of the particle channel saves significant computational resources, especially when it comes to simulating bimodal particle sets en masse with highly discretized domains.

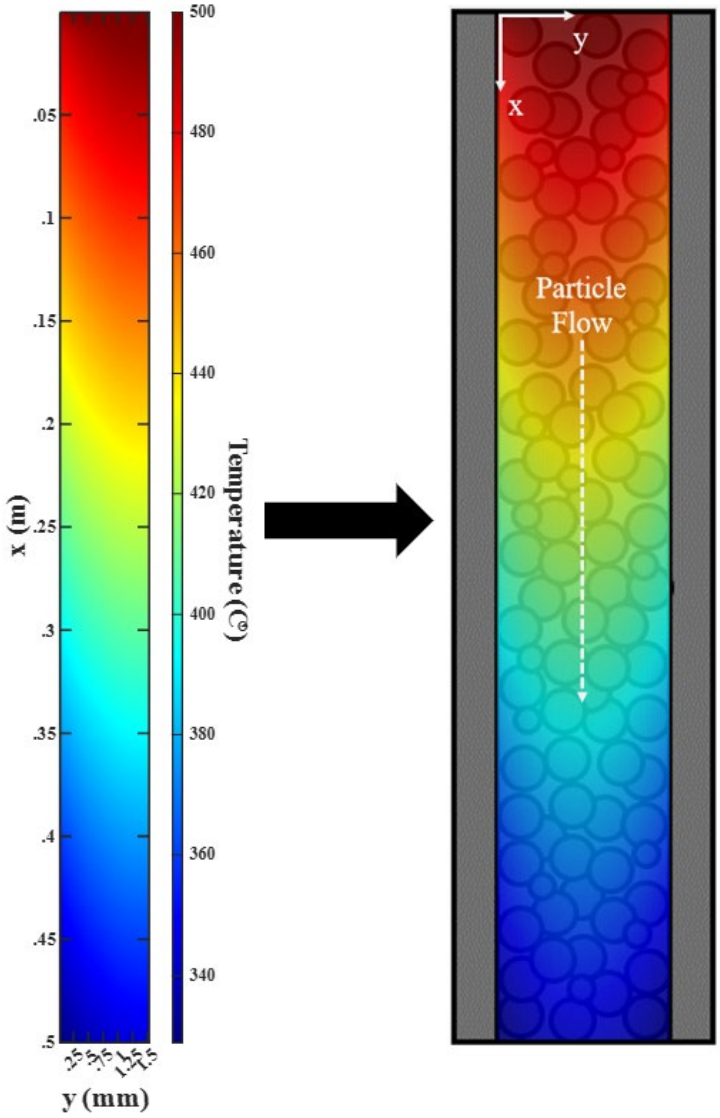

Figure 3.5 Numerically produced steady state temperature profile of HSP 40/70 particles flowing through the G3P3 20 kW_t counterflow shell-and-plate moving packed-bed heat exchanger on the left-hand side. The right illustrates the temperature profile superimposed on the entire particle channel.

SNL has experimentally tested HSP 40/70 at several different sCO_2 and particle mass flow rates in the G3P3 20 kW_t prototype heat exchanger. Found in Figure 3.6, the numerical model does a commendable job predicting the overall heat transfer coefficient at three different particle and sCO_2 flow rates for temperatures up to 500 °C using both the ZBS and the Yagi and Kunii thermal conductivity methods. With respect to Figure 3.6, the ZBS thermal conductivity method is significantly more accurate in helping

predict the overall heat transfer coefficient than the Yagi and Kunii method at the temperature range of 200-500 °C. It should be noted that ΔT_{lm} is consistent at 50 °C for each numerical simulation found in Figure 3.6. This is expected as sections 2.4.4 and 2.4.5 demonstrated with experimental data that the ZBS method more accurately characterizes thermal conductivity in the 200-500 °C range. It would be expected that experimental data at temperatures in excess of 500 °C would more closely resemble overall heat transfer coefficients calculated by using the Yagi and Kunii thermal conductivity method. The numerical model struggles to accurately predict overall heat transfer coefficients when the particle or sCO_2 mass flow rates are below 100 g/s when using either thermal conductivity method. However, when simulating at a particle and sCO_2 mass flow rate of ~100 g/s, the ZBS thermal conductivity method yields highly accurate predictions as to what the overall heat transfer coefficient will be. For this reason, binary particle distribution simulations occurring in the next section will be administered with particle and sCO_2 mass flow rates of ~100 g/s.

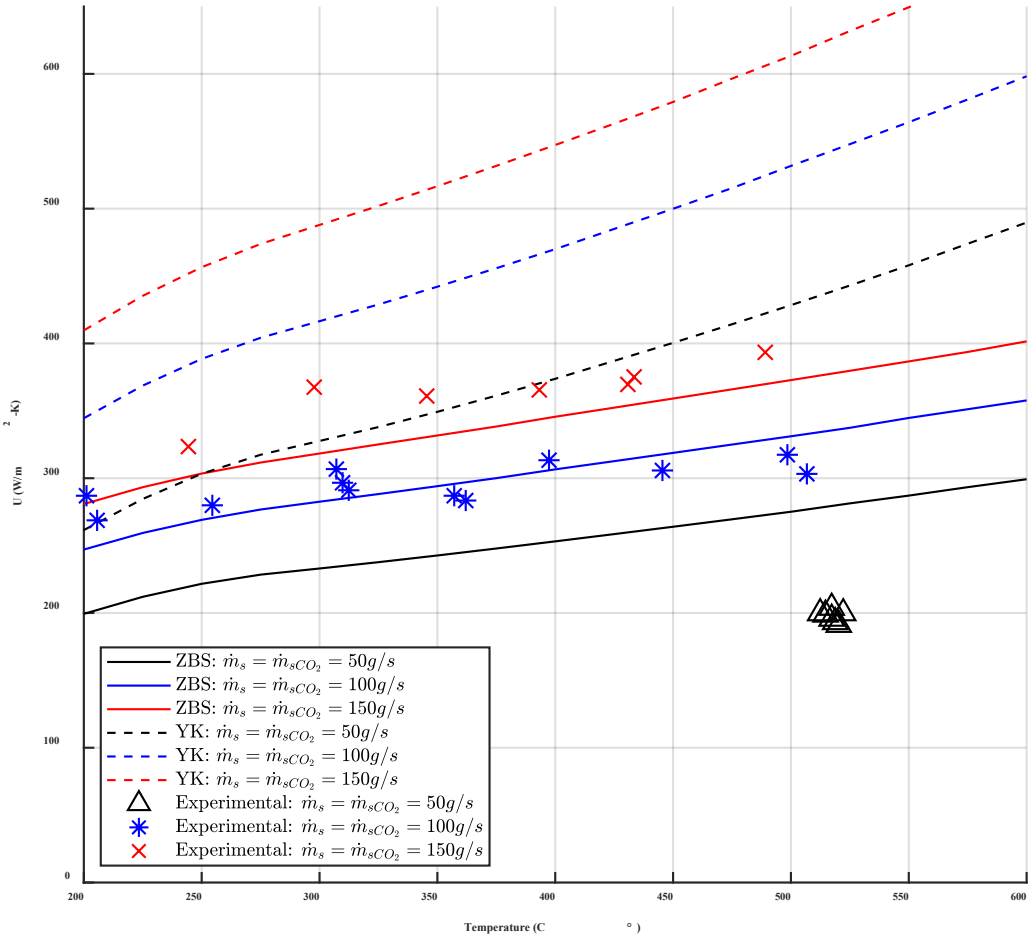

Figure 3.6 G3P3 20 kW_t prototype numerical model using both ZBS and Yagi and Kunii thermal conductivity models and SNL G3P3 20 kW_t prototype HSP 40/70 experimental data. A consistent ΔT_{lm} is utilized at 50 °C for all simulated temperatures.

3.4 Binary Particle Distribution Modeling

3.4.1 G3P3 20 kW_t Prototype Modeling with ZBS and HSP Particles

Having shown that a particle and sCO_2 mass flow rate of ~100 g/s with the ZBS yields results highly similar to G3P3 20 kW_t prototype experimental data, 100 g/s will heretofore be utilized in binary particle G3P3 20 kW_t prototype heat exchanger simulations. Consider Figure 3.7 where the binary particle mixture of HSP 16/30-40/70 is

explored with the G3P3 20 kW_t prototype model. The reader interested in overall heat transfer contour plots calculated with the Yagi and Kunii thermal conductivity method is referred to Appendix A.1 as the Yagi and Kunii method has proven to yield inaccurate results at the operating temperatures and mass flow rates of the G3P3 20 kW_t prototype heat exchanger (Figures 3.5, 2.12). In reference to Figure 3.7, attention should be directed to the white vertical lines on each plot that represent the specific HSP 16/30-40/70 particle mixture. The position of these vertical lines signifies that if HSP 16/30-40/70 were to be implemented as heat transfer media in the G3P3 20 kW_t prototype heat exchanger, an overall heat transfer coefficient improvement of up to 20% could be expected if $X_L < \sim.7$. An HSP 16/30-40/70 large particle volume fraction greater than ~.9 yields no difference in the overall heat transfer coefficient than if the mixture was pure HSP 16/30.

It should be noted that HSP 16/30 particles have a diameter of ~866 μm and that the particle channel width is only 3 mm allowing only about 3 HSP 16/30 particles to flow side by side. Larger particles (> 700 μm) when relatively compared to the diameter of the channel in which they flow have the potential to cause flowability issues and for this reason, smaller particles (< 200 μm) have been shown to yield better flowability and overall heat transfer [7], [11]. CARBOBEAD manufactures many different sizes of particles. Another binary mixture of particles manufactured by CARBOBEAD that could be used to effectively decrease monodisperse bulk porosity is the CP 20/40-70/140 mixture.

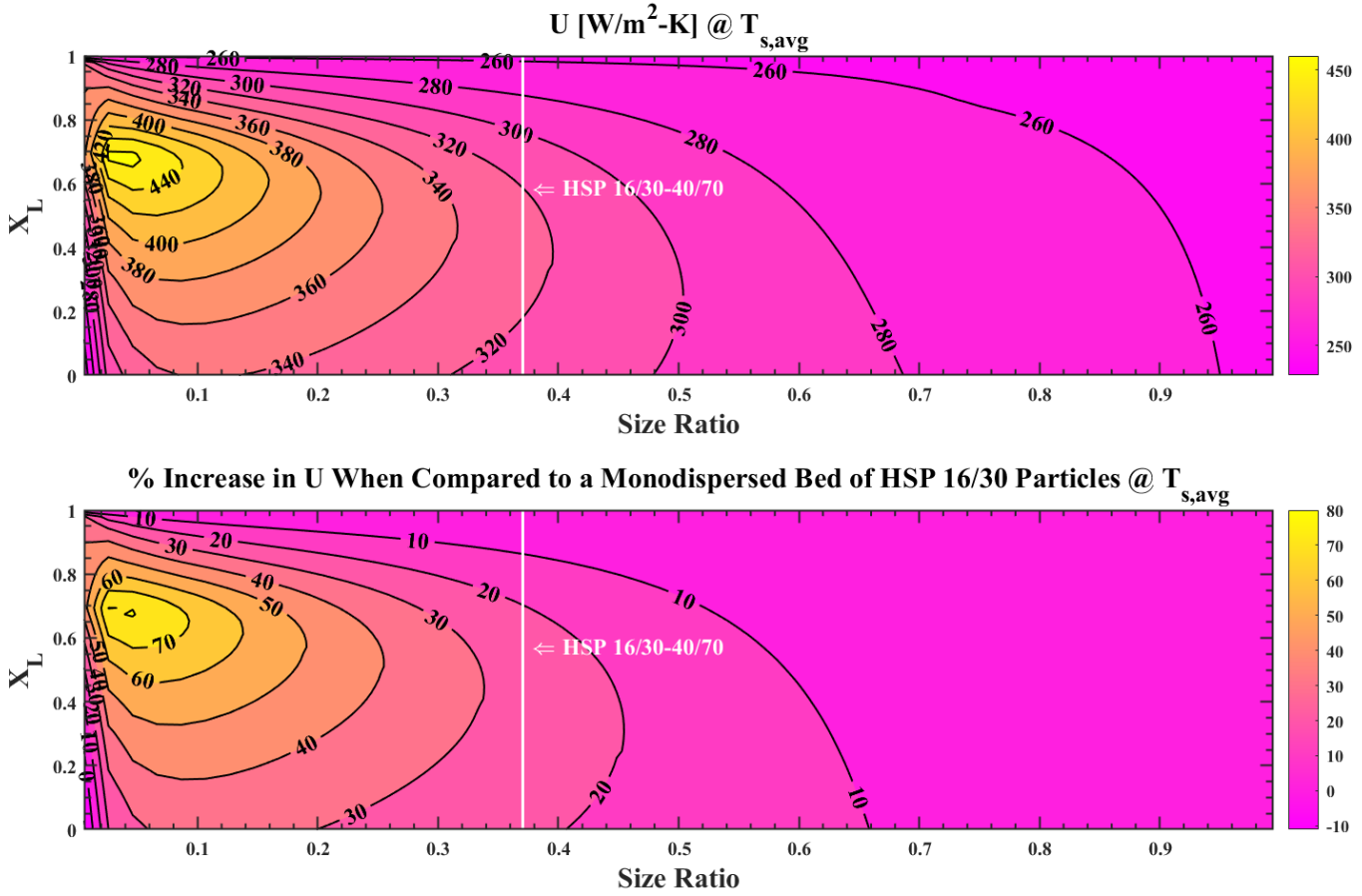

Figure 3.7 Overall heat transfer coefficient and % increase in overall heat transfer coefficient contour plots modeled in the G3P3 20 kW_t prototype heat exchanger with binary particle mixtures using a large particle size of HSP 16/30. Model uses the ZBS thermal conductivity method in the calculation of the overall heat transfer coefficient.

3.4.2 G3P3 20 kW_t Prototype Modeling with ZBS and CP Particles

CARBOBEAD CP particles are highly similar to HSP particles with the only difference, aside from the different various sizes of particles, being the absolute density. HSP particles are slightly denser at 3.61 g/cm^3 than CP particles are at 3.27 g/cm^3 [28]. Because of this, it can be expected that CP particles will perform similarly to HSP in the G3P3 20 kW_t prototype heat exchanger. A benefit of the CP particle group is that there is a larger size distribution of particles to utilize when implementing a binary mixture whereas the HSP group is fairly limited.

A promising particle mixture for use in the G3P3 20 kW_t prototype heat exchanger is the CP 20/40-70/140 particle mixture. These particles are smaller than the HSP 16/30-40/70 mixture. For reference, HSP 16/30 has a diameter of 956 μm, HSP 40/70 a 321 μm diameter, CP 20/40 a 672 μm diameter and CP 70/140 a 154 μm diameter. This smaller range of diameters available in the CP 20/40-70/140 mixture grants better flowability in smaller particle channel diameters ultimately allowing greater heat transfer. Observe Figure 3.8 illustrating the benefits of utilizing this particle distribution in the G3P3 20 kW_t prototype heat exchanger. Nearly identical to Figure 3.7, Figure 3.8 demonstrates that a CP 20/40-70/140 binary particle mixture with X_L = .2-.8 will impute approximately a 30% increase when compared to a monodisperse packed bed of CP 20/40 when used as heat transfer media in the G3P3 20 kW_t prototype heat exchanger. Furthermore, if $X_L \approx .6$, nearly a 40% improvement in the overall heat transfer coefficient can be expected when compared to monodisperse packed bed of CP 20/40 in the G3P3 20 kW_t prototype heat exchanger.

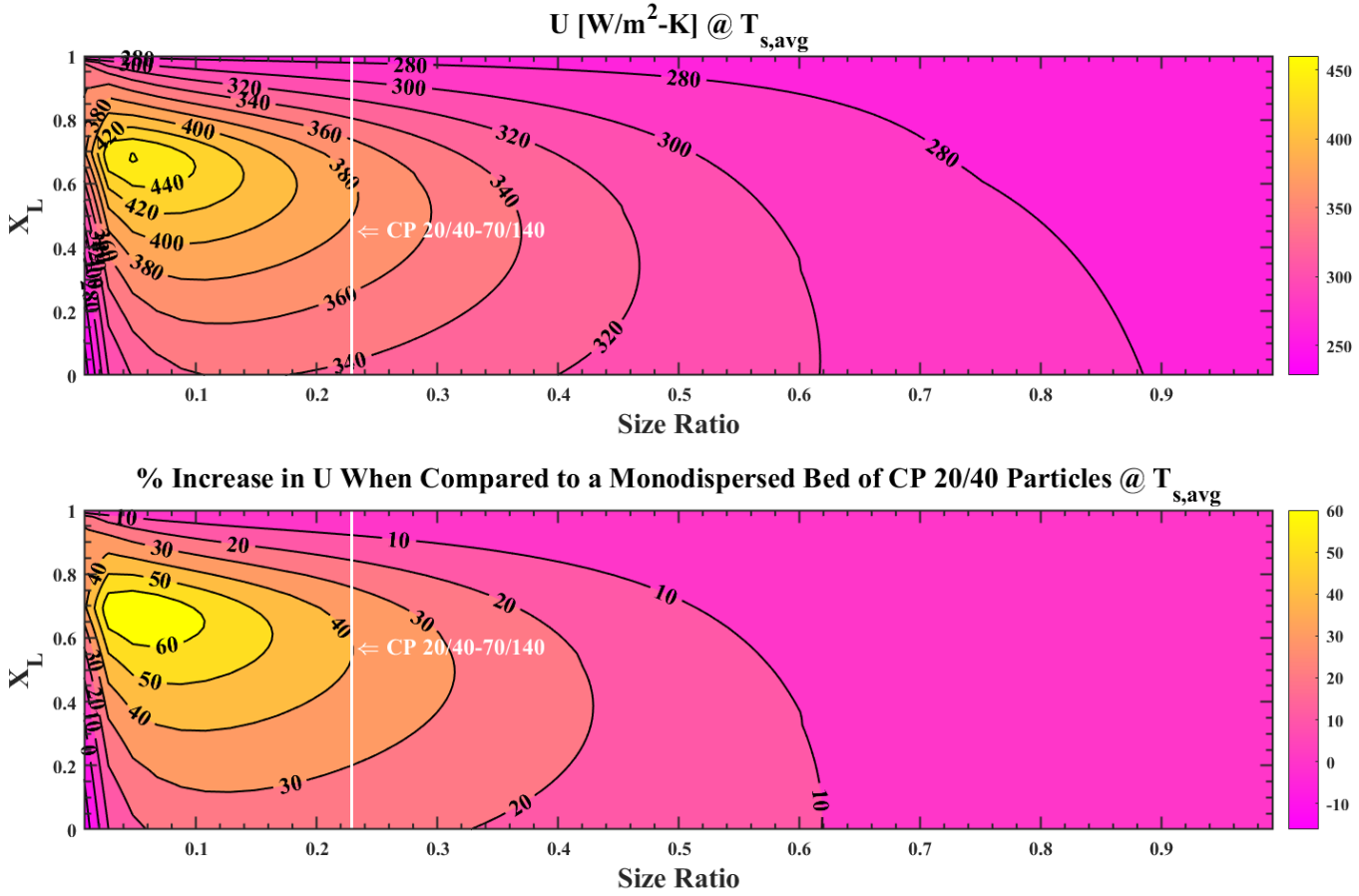

Figure 3.8 Overall heat transfer coefficient and % increase in overall heat transfer coefficient contour plots modeled in the G3P3 20 kW_t prototype heat exchanger with binary particle mixtures using a large particle size of CP 20/40. Model uses the ZBS thermal conductivity method in the calculation of the overall heat transfer coefficient.

CHAPTER FOUR: CONCLUSIONS

This work contributes to the area of solid particles used as heat transfer media because it explores how the thermal conductivity of already-in-use solid particle media can be cheaply and efficiently improved. It is unique to other studies because binary particle systems have not been examined at temperatures above 300 °C. It is also unique because binary particle systems have not been examined with a load imposed upon them.

Multiple large particle volume fractions of a binary mixture composed of HSP 16/30 and HSP 40/70 CARBOBEADs were analyzed at temperatures from 300-700 °C. Using the obtained data, comparisons were made to the predictions of two thermal conductivity models: ZBS and Yagi and Kunii. Each of these thermal conductivity models was analyzed with two porosity models: the Standish and Yu and the Chang and Deng. It was found that at temperatures above ~400 °C, a monodispersed particle distribution composed of larger particles yields the highest thermal conductivity. It was also determined that the ZBS thermal conductivity model is better suited to predict the thermal conductivity of binary and monodispersed particle distributions up to around ~400 °C. Above 500 °C, it was determined that the Yagi and Kunii thermal conductivity model was better suited to predict the thermal conductivity of binary and monodispersed particle distributions. For temperatures of 700 °C and above, neither thermal conductivity model was capable of accurately predicting the behavior of binary and monodispersed particle distributions. It was concluded that binary particle distributions under load have increases in thermal conductivity of ~1-2% more than increases in monodispersed

particle distributions under the same load. Overall, particle distributions under load can be expected to see up to nearly a 10% increase in thermal conductivity if properly executed.

It was also concluded that measurement technique is important in determining the thermal conductivity of a particle distribution. Fresh particle testing (where particles are replaced after each test) showed a 3-4% variation in thermal conductivity readings while the stale particle testing (where particles are replaced after each test) variation equated to roughly 1-2%. Recalling the ~1% variation across 10 bulk porosity measurements calculated for each particle distribution (see Table 2.1), it is not likely that the larger variation in thermal conductivity is attributed to bulk porosity variation but to near wall porosity variation (i.e., at the sensor-particle interface). While the bulk porosity of particle distributions is generally understood and documented, near wall porosity and the effects it has on the thermal conductivity of a particle distribution is not. Attempts to further understand this behavior with modulated photothermal radiometry (MPTR) have potential [15], [70], however more work is needed in this area.

A numerical model of the SNL's G3P3 20 kW_t prototype heat exchanger was implemented and validated with G3P3 20 kW_t prototype heat exchanger experimental data from SNL at particle and sCO_2 mass flow rates of 100 g/s with the aid of the ZBS thermal conductivity method. Analysis of simulation and experimental data revealed that at particle and sCO_2 mass flow rates of 100 g/s the ZBS is an appropriate thermal conductivity method to utilize at G3P3 20 kW_t prototype heat exchanger at working temperatures (290-500 °C) and the Yagi and Kunii thermal conductivity is not. Using the validated flow rates and thermal conductivity method, G3P3 20 kW_t prototype heat

exchanger simulation data revealed potential increases in the overall heat transfer coefficient of up to 25% in HSP 16/30-40/70 mixtures and as high as 40% in CP 20/40-70/140 mixtures when implementing the optimal large particle volume fraction. This knowledge is critical to the entire CSP industry as Sandia National Laboratory continues to spearhead the research and development of the world's first 1 MW_t heat exchanger under the Gen3 Particle Pilot Plant (G3P3) program.

CHAPTER FIVE: FUTURE WORK

Chapter 2 of this work explored and analyzed the thermal conductivity of bimodal particle distributions at high temperatures revealing that bimodal particle distributions are only beneficial up until ~400 °C, the same temperature at which the ZBS can adequately evaluate the thermal conductivity of a particle distribution.

Chapter 3 of this work derived, defined, simulated and validated a G3P3 20 kW_t prototype heat exchanger model that can effectively predict the overall heat transfer coefficient of a particular heat transfer media when utilizing particle and sCO_2 mass flow rates of 100 g/s and the ZBS thermal conductivity method at working G3P3 20 kW_t prototype heat exchanger temperatures (290-500 °C). Simulations indicated potential increases in the overall heat transfer coefficient of up to 25% in HSP 16/30-40/70 mixtures and as high as 40% in CP 20/40-70/140 mixtures when implementing the optimal large particle volume fraction. While the HSP 16/30-40/70 mixture exceeds the size limit for heat transfer media in the G3P3 20 kW_t prototype heat exchanger, CP 20/40-70/140 is a viable option and should be utilized. The experimental data from the CP 20/40-70/140 G3P3 20 kW_t prototype heat exchanger will help to validate the numerical model, the ZBS thermal conductivity method and cement the heat transfer superiority of bimodal particle distributions at G3P3 20 kW_t prototype heat exchanger working temperatures.

REFERENCES

[1] Polybius, The Histories, Trans. W. R. Paton (London, 1923), 3:453-59 (Attack By Sea), 461-63 (Attack By Land) (8. 2. 3.2-8.4), 537-39 (Capture Of The City) (8. 6. 37); Titus Livius, Trans. F. G. Moore (London, 1966), 6:283-87 (214 B.C. Siege) (24. 34), 461 (212 B.C. Death) (25. 31. 9-10).

[2] D. L. Simms, "Archimedes And The Burning Mirrors Of Syracuse," 1977. [Online]. Available: Https://About.Jstor.Org/Terms.

[3] Jan Null (2009) Harnessing The Sun".As N Null(2009)Harnessing The Sun:The Promises Of Solar Energy,Weatherwise,62:4,30-36,DOI:10.3200/WEWI.62.4.30-36.

[4] Dittmann, Frank.Frank Shuman And The Early Utilization Of The Solar Power. Beginnings Of The Solar Power; Frank Shuman Und Die Fruehe Nutzung Der Solarenergie. Anfaenge Der Solarenergie.Germany: N. P., 2013. Web.

[5] Samaan Ladkany, William Culbreth, And Nathan Loyd, "Molten Salts And Applications I: Molten Salt History, Types, Thermodynamic And Physical Properties, And Cost," *Journal Of Energy And Power Engineering*, Vol. 12, No. 11, Nov. 2018, Doi: 10.17265/1934-8975/2018.11.001.

[6] Silvi, Cesare. (2005). The Work Of Italian Solar Energy Pioneer Giovanni Francia (1911-1980).

[7] M. Mehos *Et Al.*, "Concentrating Solar Power Gen3 Demonstration Roadmap," 1980. [Online]. Available: Www.Nrel.Gov/Publications.

[8] N. P. Siegel, M. D. Gross, And R. Coury, "The Development Of Direct Absorption And Storage Media For Falling Particle Solar Central Receivers," *Journal Of Solar*

Energy Engineering, Transactions Of The ASME, Vol. 137, No. 4, 2015, Doi: 10.1115/1.4030069.

[9] A. G. Fernández, J. Gomez-Vidal, E. Oró, A. Kruizenga, A. Solé, And L. F. Cabeza, "Mainstreaming Commercial CSP Systems: A Technology Review," *Renewable Energy*, Vol. 140. Elsevier Ltd, Pp. 152–176, Sep. 01, 2019. Doi: 10.1016/J.Renene.2019.03.049.

[10] C. K. Ho, M. Carlson, K. J. Albrecht, Z. Ma, S. Jeter, And C. M. Nguyen, "Evaluation Of Alternative Designs For A High Temperature Particle-To-Sco 2 Heat Exchanger," *Journal Of Solar Energy Engineering, Transactions Of The ASME*, Vol. 141, No. 2, Apr. 2019, Doi: 10.1115/1.4042225.

[11] K. J. Albrecht And C. K. Ho, "Design And Operating Considerations For A Shell-And-Plate, Moving Packed-Bed, Particle-To-Sco2 Heat Exchanger," *Solar Energy*, Vol. 178, Pp. 331–340, Jan. 2019, Doi: 10.1016/J.Solener.2018.11.065.

[12] K. J. Albrecht And C. K. Ho, "High-Temperature Flow Testing And Heat Transfer For A Moving Packed-Bed Particle/Sco2 Heat Exchanger," In *AIP Conference Proceedings*, American Institute Of Physics Inc., Nov. 2018. Doi: 10.1063/1.5067039.

[13] Calderón, A,Barreneche, C,Palacios, A, Et Al.Review Of Solid Particle Materials For Heat Transfer Fluid And Thermal Energy Storage In Solar Thermal Power Plants.Energy Storage.2019;1:E63.Https://Doi.Org/10.1002/Est2.63.

[14] T. Baumann And S. Zunft, "Properties Of Granular Materials As Heat Transfer And Storage Medium In CSP Application," *Solar Energy Materials And Solar Cells*, Vol. 143, Pp. 38–47, Jul. 2015, Doi: 10.1016/J.Solmat.2015.06.037.

[15] J. Zeng *Et Al.*, “Measurement Of High-Temperature Thermophysical Properties Of Bulk And Coatings Using Modulated Photothermal Radiometry,” *Int J Heat Mass Transf*, Vol. 170, May 2021, Doi: 10.1016/J.Ijheatmasstransfer.2021.120989.

[16] E. S. Toberer, L. L. Baranowski, And C. Dames, “Advances In Thermal Conductivity,” *Annual Review Of Materials Research*, Vol. 42. Pp. 179–209, Aug. 2012. Doi: 10.1146/Annurev-Matsci-070511-155040.

[17] S. Trevisan, W. Wang, And B. Laumert, “Coatings Utilization To Modify The Effective Properties Of High Temperature Packed Bed Thermal Energy Storage,” *Appl Therm Eng*, Vol. 185, Feb. 2021, Doi: 10.1016/J.Applthermaleng.2020.116414.

[18] J. Yin, Q. Zheng, And X. Zhang, “Heat Transfer Model Of A Particle Energy Storage-Based Moving Packed Bed Heat Exchanger,” *Energy Storage*, Vol. 2, No. 1, Feb. 2020, Doi: 10.1002/Est2.113.

[19] H. Disk, “Application Note Nr.7 From Hot Disk Applications,” PR China, 2000. [Online]. Available: Www.Hotdisk.Se.

[20] Z. Wang *Et Al.*, “Aluminum And Silicon Based Phase Change Materials For High Capacity Thermal Energy Storage,” *Appl Therm Eng*, Vol. 89, Pp. 204–208, Jun. 2015, Doi: 10.1016/J.Applthermaleng.2015.05.037.

[21] K. M. Chung And R. Chen, “Black Coating Of Quartz Sand Towards Low-Cost Solar-Absorbing And Thermal Energy Storage Material For Concentrating Solar Power,” *Solar Energy*, Vol. 249, Pp. 98–106, Jan. 2023, Doi: 10.1016/J.Solener.2022.11.028.

[22] E. Gietzen, S. Karimi, N. Goel, S. A. Shirazi, M. Keller, And T. Otanicar, “Experimental Investigation Of Low Velocity And High Temperature Solid Particle Impact Erosion Wear,” *Wear*, Vol. 506–507, Oct. 2022, Doi: 10.1016/J.Wear.2022.204441.

[23] C. E. Christen, J. Gómez-Hernández, And T. P. Otanicar, “Bimodal Particle Distributions With Increased Thermal Conductivity For Solid Particles As Heat Transfer Media And Storage Materials,” *Int J Heat Mass Transf*, Vol. 184, Mar. 2022, Doi: 10.1016/J.Ijheatmasstransfer.2021.122250.

[24] Yu, A.B. (07/1988). "An Analytical—Parametric Theory Of The Random Packing Of Particles".Powder Technology(0032-5910), 55 (3), P. 171.

[25] C. S. Chang And Y. Deng, “A Nonlinear Packing Model For Multi-Sized Particle Mixtures,” *Powder Technol*, Vol. 336, Pp. 449–464, Aug. 2018, Doi: 10.1016/J.Powtec.2018.06.008.

[26] Schlunder, Effective Radial Thermal Conductivity Of Packings In Gas Flow. Part II Thermal Conductivity Of The Packing Fraction Without Gas Flowr Bauer-International Chemical Engineering, 1978.

[27] S. Yagi And D. Kunii, “Studies On Effective Thermal Conductivities In Packed Beds,” Al, Vol. 3, No. 3, Pp. 373–381, 1957.

[28] CARBO, “CARBOBEAD Technical Data Sheet,” 2019. [Online]. Available: Https://Carboceramics.Com/Getmedia/F3f7794b-9cd4-4a8f-8184-93eb75f5bddd/CARBOBEAD-Technical-Data-Sheet-1001_317v5.Pdf?Ext=.Pdf.

[29] K. M. Chung *Et Al.*, “Measurement And Analysis Of Thermal Conductivity Of Ceramic Particle Beds For Solar Thermal Energy Storage,” *Solar Energy*

Materials And Solar Cells, Vol. 230, Sep. 2021, Doi: 10.1016/J.Solmat.2021.111271.

[30] M. V. Bagepalli, J. D. Yarrington, A. J. Schrader, Z. M. Zhang, D. Ranjan, And P. G. Loutzenhiser, "Measurement Of Flow Properties Coupled To Experimental And Numerical Analyses Of Dense, Granular Flows For Solar Thermal Energy Storage," *Solar Energy*, Vol. 207, Pp. 77–90, Sep. 2020, Doi: 10.1016/J.Solener.2020.06.062.

[31] P. B. Kowalczuk And J. Drzymala, "Physical Meaning Of The Sauter Mean Diameter Of Spherical Particulate Matter," *Particulate Science And Technology*, Vol. 34, No. 6, Pp. 645–647, Nov. 2016, Doi: 10.1080/02726351.2015.1099582.

[32] Tsotsas, Evangelos (12/1991). "Impact Of Particle Size Dispersity On Thermal Conductivity Of Packed Beds: Measurement, Numerical Simulation, Prediction".Chemical Engineering & Technology(0930-7516), 14 (6), P. 421.

[33] Measurement Acceptance Criteria. [Online]. Available: Https://Gen3csp.Gatech.Edu/Criteria/.

[34] A. Gunawan And G. W. Woodruff, "Uncertainty Analysis And Error Propagation Methodology For Reporting Thermophysical Properties Measurement Of Gen3 CSP Materials."

[35] R. K. Mcgeary, (10/1961). "Mechanical Packing Of Spherical Particles". Journal Of The American Ceramic Society(0002-7820), 44 (10), P. 513.

[36] R. Y. Yang, R. P. Zou, And A. B. Yu, "Computer Simulation Of The Packing Of Fine Particles," VOLUME 62, NUMBER 3. *The American Physical Society*. Sept. 2000.

[37] K. J. Albrecht And C. K. Ho, “Heat Transfer Models Of Moving Packed-Bed Particle-To-Sco2 Heat Exchangers,” *Journal Of Solar Energy Engineering, Transactions Of The ASME*, Vol. 141, No. 3, Jun. 2019, Doi: 10.1115/1.4041546.

[38] W. Van Antwerpen, C. G. Du Toit, And P. G. Rousseau, “A Review Of Correlations To Model The Packing Structure And Effective Thermal Conductivity In Packed Beds Of Mono-Sized Spherical Particles,” *Nuclear Engineering And Design*, Vol. 240, No. 7. Pp. 1803–1818, Jul. 2010. Doi: 10.1016/J.Nucengdes.2010.03.009.

[39] Hsu, C.T. (11/1994). "Modified Zehner-Schlunder Models For Stagnant Thermal Conductivity Of Porous Media". International Journal Of Heat And Mass Transfer(0017-9310), 37 (17), P. 2751.

[40] Z. Peng, E. Doroodchi, And B. Moghtaderi, “Heat Transfer Modelling In Discrete Element Method (DEM)-Based Simulations Of Thermal Processes: Theory And Model Development,” *Prog Energy Combust Sci*, Vol. 79, Jul. 2020, Doi: 10.1016/J.Pecs.2020.100847.

[41] M. Moscardini, Y. Gan, S. Pupeschi, And M. Kamlah, “Discrete Element Method For Effective Thermal Conductivity Of Packed Pebbles Accounting For The Smoluchowski Effect,” *Fusion Engineering And Design*, Vol. 127, Pp. 192–201, Feb. 2018, Doi: 10.1016/J.Fusengdes.2018.01.013.

[42] G. Zanganeh, A. Pedretti, A. Haselbacher, And A. Steinfeld, “Design Of Packed Bed Thermal Energy Storage Systems For High-Temperature Industrial Process Heat,” *Appl Energy*, Vol. 137, Pp. 812–822, Jan. 2015, Doi: 10.1016/J.Apenergy.2014.07.110.

[43] W. Van Antwerpen, C. G. Du Toit, And P. G. Rousseau, “A Review Of Correlations To Model The Packing Structure And Effective Thermal Conductivity In Packed Beds Of Mono-Sized Spherical Particles,” *Nuclear Engineering And Design*, Vol. 240, No. 7. Pp. 1803–1818, Jul. 2010. Doi: 10.1016/J.Nucengdes.2010.03.009.

[44] Holman, Jack P. Heat Transfer. Mcgraw Hill Higher Education, 2010.

[45] A. Karim, J. Bravo, And A. Datye, “Nonisothermality In Packed Bed Reactors For Steam Reforming Of Methanol,” *Appl Catal A Gen*, Vol. 282, No. 1–2, Pp. 101–109, Mar. 2005, Doi: 10.1016/J.Apcata.2004.12.006.

[46] A. Zbogar, F. J. Frandsen, P. A. Jensen, And P. Glarborg, “Heat Transfer In Ash Deposits: A Modelling Tool-Box,” *Progress In Energy And Combustion Science*, Vol. 31, No. 5–6. Pp. 371–421, 2005. Doi: 10.1016/J.Pecs.2005.08.002.

[47] Y. Qian, Z. Han, J. H. Zhan, X. Liu, And G. Xu, “Comparative Evaluation Of Heat Conduction And Radiation Models For CFD Simulation Of Heat Transfer In Packed Beds,” *Int J Heat Mass Transf*, Vol. 127, Pp. 573–584, Dec. 2018, Doi: 10.1016/J.Ijheatmasstransfer.2018.06.127.

[48] Denloye, A. O. O., And J. S. M. Botterill. "A Theoretical Model Of Heat Transfer To A Packed Or Quiescent Fluidized Bed."Chem. Eng. Sci.33 (1978): 509-515.

[49] Navidi, William Cyrus, And Navidi, William. Statistics For Engineers And Scientists. United Kingdom, Mcgraw-Hill, 2011.

[50] A. Rosato, K. 3 Strandburg, F. Prinz, And R. H. Swendsen, “Why The Brazil Nuts Are On Top: Size Segregation Of Particulate Matter By Shaking.”

[51] C. K. Ho, “A Review Of High-Temperature Particle Receivers For Concentrating Solar Power,” *Applied Thermal Engineering*, Vol. 109. Elsevier Ltd, Pp. 958–969, Oct. 25, 2016. Doi: 10.1016/J.Applthermaleng.2016.04.103.

[52] J. M. Yin, Q. Y. Zheng, Z. R. Peng, And X. R. Zhang, “Review Of Supercritical CO2 Power Cycles Integrated With CSP,” *International Journal Of Energy Research*, Vol. 44, No. 3. John Wiley And Sons Ltd, Pp. 1337–1369, Mar. 10, 2020. Doi: 10.1002/Er.4909.

[53] Z. Ma And J. Martinek, “Fluidized-Bed Heat Transfer Modeling For The Development Of Particle/Supercritical-CO2 Heat Exchanger,” In ASME 2017 11th International Conference On Energy Sustainability, 2017.

[54] T. Baumann And S. Zunft, “Development And Performance Assessment Of A Moving Bed Heat Exchanger For Solar Central Receiver Power Plants,” In *Energy Procedia*, Elsevier Ltd, May 2015, Pp. 748–757. Doi: 10.1016/J.Egypro.2015.03.085.

[55] K. J. Albrecht, M. D. Carlson, H. F. Laubscher, R. Crandell, N. Delovato, And C. K. Ho, “Testing And Model Validation Of A Prototype Moving Packed-Bed Particle-To-Sco2 Heat Exchanger,” *In proceedings of the 7th international conference on electronic devices, systems and applications (icedsa2020)*, AIP Publishing, Dec. 2020, P. 030002. Doi: 10.1063/5.0031483.

[56] K. J. Albrecht, H. F. Laubscher, C. P. Bowen, And C. K. Ho, “SANDIA REPORT Performance Evaluation Of A Prototype Moving Packed-Bed Particle/Sco 2 Heat Exchanger.” [Online]. Available: Https://Classic.Ntis.Gov/Help/Order-Methods.

[57] B. H. Mills, C. K. Ho, N. R. Schroeder, R. Shaeffer, H. F. Laubscher, And K. J. Albrecht, “Design Evaluation Of A Next-Generation High-Temperature Particle Receiver For Concentrating Solar Thermal Applications,” *Energies*, Vol. 15, No. 5. MDPI, Mar. 01, 2022. Doi: 10.3390/En15051657.

[58] C. K. Ho *Et Al.*, “Receiver Design And On-Sun Testing For G3P3-USA,” In *AIP Conference Proceedings*, American Institute Of Physics Inc., May 2022. Doi: 10.1063/5.0086071.

[59] V. Pandey, P. Kumar, And P. Dutta, “Thermo-Hydraulic Analysis Of Compact Heat Exchanger For A Simple Recuperated Sco2 Brayton Cycle,” *Renewable And Sustainable Energy Reviews*, Vol. 134, Dec. 2020, Doi: 10.1016/J.Rser.2020.110091.

[60] R. Henda And D. J. Falcioni, “Modeling Of Heat Transfer In A Moving Packed Bed: Case Of The Preheater In Nickel Carbonyl Process,” In *Journal Of Applied Mechanics, Transactions ASME*, Jan. 2006, Pp. 47–53. Doi: 10.1115/1.1991862.

[61] A. Denloye And J. Botterill, “A Theoretical Model Of Heat Transfer To A Packed Or

Quiescent Fluidized Bed,” Chem. Eng. Sci., Vol. 33, No. 4, Pp. 509–515, 1978.

[62] A. G. Dixon, A. K. Gurnon, M. Nijemeisland, And E. H. Stitt, “CFD Testing Of The Pointwise Use Of The Zehner-Schlünder Formulas For Fixed-Bed Stagnant Thermal Conductivity,” *International Communications In Heat And Mass Transfer*, Vol. 42, Pp. 1–4, Mar. 2013, Doi: 10.1016/J.Icheatmasstransfer.2012.12.013.

[63] V. Gnielinski, “New Equations For Heat And Mass Transfer In Turbulent Pipe And Channel Flow,” Int. Chem. Eng., Vol. 16, No. 2, Pp. 359–367, 1976.

[64] R. Span And W. Wagner, “A New Equation Of State For Carbon Dioxide Covering The Fluid Region From The Triple-Point Temperature To 1100 K At Pressures Up To 800 Mpa,” *J Phys Chem Ref Data*, Vol. 25, No. 6, Pp. 1509–1596, 1996, Doi: 10.1063/1.555991.

[65] Y. S. Muzychka, E. Walsh, And P. Walsh, “Simple Models For Laminar Thermally Developing Slug Flow In Noncircular Ducts And Channels,” *J Heat Transfer*, Vol. 132, No. 11, 2010, Doi: 10.1115/1.4002095.

[66] Watkins, M.F., Gould, R.D., 2017. Heat Transfer To Vertical Dense Granular Flows At High Operating Temperatures, In: ASME 2017 11th International Conference On Energy Sustainability. American Society Of Mechanical Engineers. Https://Doi.Org/10.1115/ES2017-3272.

[67] Holman, J.P., 2010. Heat Transfer, 10th Ed. Mcgaw-Hill, New York.

[68] K. J. Albrecht And C. K. Ho, “Heat Transfer Models Of Moving Packed-Bed Particle-To-Sco2 Heat Exchangers,” *Journal Of Solar Energy Engineering, Transactions Of The ASME*, Vol. 141, No. 3, Pp. 1–10, 2017, Doi: 10.1115/1.4041546.

[69] J. Corona, D. Stout, T. P. Otanicar, And N. Kandadai, “Characterizing Particle-Based Thermal Storage Performance Using Optical Methods For Use In Next Generation Concentrating Solar Power Plants,” SPIE-Intl Soc Optical Eng, Sep. 2022, P. 21. Doi: 10.1117/12.2632268.